Rapid #: -21327889

CROSS REF ID: **32297853710001852**

LENDER: **TWHRI (National Health Research Institutes) :: Main Library**

BORROWER: **ORU (University of Oregon) :: Main Library**

TYPE:	Article CC:CCL
JOURNAL TITLE:	Journal of metamorphic geology
USER JOURNAL TITLE:	Journal of Metamorphic Geology
ARTICLE TITLE:	Internally consistent data for sulphur-bearing phases and application to the construction of pseudosections for mafic greenschist facies rocks in Na2O-CaO-K2O-FeO-MgO-Al2O3-SiO2-CO2-O-S-H2O
ARTICLE AUTHOR:	EVANS, K A
VOLUME:	28
ISSUE:	6
MONTH:	
YEAR:	2010
PAGES:	667 - 687
ISSN:	0263-4929
OCLC #:	

Processed by RapidX: 9/25/2023 8:51:57 PM

Journal of
METAMORPHIC GEOLOGY

J. metamorphic Geol., 2010, **28,** 667–687 doi:10.1111/j.1525-1314.2010.00890.x

Internally consistent data for sulphur-bearing phases and application to the construction of pseudosections for mafic greenschist facies rocks in Na_2O–CaO–K_2O–FeO–MgO–Al_2O_3–SiO_2–CO_2–O–S–H_2O

K. A. EVANS,[1] R. POWELL[2] AND T. J. B.HOLLAND[3]

[1] *Department of Applied Geology, Curtin University, GPO Box U1987, Bentley, WA 6845, Australia (k.evans@curtin.edu.au)*

[2] *School of Earth Sciences, Melbourne University, Melbourne, Australia*

[3] *Department of Earth Sciences, University of Cambridge, Downing Street, Cambridge, UK*

ABSTRACT The Holland and Powell internally consistent data set version 5.5 has been augmented to include pyrite, troilite, trov ($Fe_{0.875}S$), anhydrite, H_2S, elemental S and S_2 gas. Phase changes in troilite and pyrrhotite are modelled with a combination of multiple end-members and a Landau tricritical model. Pyrrhotite is modelled as a solid solution between hypothetical end-member troilite (trot) and $Fe_{0.875}S$ (trov); observed activity–composition relationships fit well to a symmetric formalism model with a value for $w_{trot-trov}$ of −3.19 kJ mol^{-1}. The hypothetical end-member approach is required to compensate for iron distribution irregularities in compositions close to troilite. Mixing in fluids is described with the van Laar asymmetric formalism model with a_{ij} values for H_2O–H_2S, H_2S–CH_4 and H_2S–CO_2 of 6.5, 4.15 and 0.045 kJ mol^{-1} respectively. The derived data set is statistically acceptable and replicates the input data and data from experiments that were not included in the initial regression. The new data set is applied to the construction of pseudosections for the bulk composition of mafic greenschist facies rocks from the Golden Mile, Kalgoorlie, Western Australia. The sequence of mineral assemblages is replicated successfully, with observed assemblages predicted to be stable at $X(CO_2)$ increasing with increasing degree of hydrothermal alteration. Results are compatible with those of previous work. Assemblages are insensitive to the S bulk content at S contents of less than 1 wt%, which means that volatilization of S-bearing fluids and sulphidation are unlikely to have had major effects on the stable mineral assemblage in less metasomatized rocks. The sequence of sulphide and oxide phases is predicted successfully and there is potential to use these phases qualitatively for geobarometry. Increases in $X(CO_2)$ stabilized, in turn, pyrite–magnetite, pyrite–hematite and anhydrite–pyrite. Magnetite–pyrrhotite is predicted at temperatures greater than 410 °C. The prediction of a variety of sulphide and oxide phases in a rock of fixed bulk composition as a function of changes in fluid composition and temperature is of particular interest because it has been proposed that such a variation in phase assemblage is produced by the infiltration of multiple fluids with contrasting redox state. The work presented here shows that this need not be the case.

Key words: gold; Kalgoorlie; redox; sulphides; sulphur; thermodynamics.

INTRODUCTION

Fluids in metamorphic systems control rheological and geochemical aspects of large proportions of the Earth's crust (e.g. Etheridge *et al.*, 1983; McCaig, 1988), and are implicated in the formation of hydrothermal ore deposits (e.g. Phillips & Brown, 1987). Direct observation of fluids in these systems is generally impractical; so, thermodynamic models form an integral part of the interpretation of metamorphic and hydrothermally altered rocks (e.g. White *et al.*, 2003). Such models allow the effects of changes in variables such as pressure, temperature, bulk and fluid composition to be predicted from forward models (e.g. Powell *et al.*, 1998), and conclusions on conditions of metamorphism may be drawn from inverse models (e.g. Powell & Holland, 2008).

Sulphur-bearing phases, such as pyrrhotite and pyrite, are widespread in metamorphic rocks (e.g. Powell *et al.*, 1991; Neumayr *et al.*, 2008), sensitive indicators of parameters that include fluid composition and temperature (e.g. Neall & Phillips, 1987; Palin & Xu, 2000) and recognized as vectors to ore in hydrothermal ore deposits (e.g. McCuaig & Kerrich, 1998). However, these phases have been difficult to incorporate rigorously into previous thermodynamic models (e.g. Johnson *et al.*, 1992; Shvarov & Bastrakov, 1999). This is because the sulphur-bearing phases exhibit complexity that cannot be replicated by simple mineral equations of state and ideal activity–composition

models. Principal issues for common phases in the system Fe–S are the multiple phase changes undergone by troilite and the pyrrhotite solid solution series at temperatures of geological interest (e.g. Grønvold *et al.*, 1959; Grønvold *et al.*, 1991; Grønvold & Stølen, 1992), and the non-ideal mixing thermodyamic of pyrrhotite (e.g. Rau, 1976; Powell, 1983). Additionally, sulphur-bearing fluid components mix non-ideally in aqueous fluids (e.g. Kishima, 1989) and may dissociate to form charged species such as HS^- (e.g. Suleimenov & Seward, 1997; Phillips & Phillips, 2000). Coherent approaches to aqueous mixed solvent solutions have been devised (e.g. Pitzer & Simonson, 1986; Anderko *et al.*, 2002; Wang *et al.*, 2002; Evans & Powell, 2006) but are not used widely in geological applications. Further complexities are provided by the presence of sulphide melts in systems where an appropriate flux for such melting is present (e.g. Tomkins *et al.*, 2007), unmixing of sulphide melts as temperatures decrease (Waldner & Pelton, 2005) and the poorly constrained nature of phase relationships between phases such as $Fe_{11}S_{12}$, $Fe_{10}S_{11}$, Fe_9S_{10}, $Fe_{7.016}S_8$ below 325 °C (e.g. Wang & Salveson, 2005). A lack of internal consistency in end-member thermodynamic data for the sulphur-bearing phases may also compromise the models.

Fortunately, much experimental effort has been devoted to the elucidation of the thermodynamic properties and phase relationships of the common sulphur-bearing phases (e.g. Rosenqvist, 1954; Dickson *et al.*, 1962; Barton & Toulmin, 1964; Toulmin & Barton, 1964; Rau, 1976; Lin *et al.*, 1977). The experimental data have been compiled and reviewed by a number of authors (e.g. Mills, 1974; Barker & Parks, 1986; Robie & Hemingway, 1995; Wang & Salveson, 2005) and data in the Fe–S system have been optimized to give internally consistent values for enthalpies and entropies of phases that include troilite, pyrite, pyrrhotite, iron, iron sulphide liquid and the stoichiometric compounds $Fe_{11}S_{12}$, $Fe_{10}S_{11}$, Fe_9S_{10}, $Fe_{7.016}S_8$ (Waldner & Pelton, 2005). The latter, however, is aimed at the material science field, and has not been calibrated for use at pressures above 1 bar, and phase changes in pyrrhotite are dealt with by discontinuities in heat capacity. The latter feature makes the model inconvenient to apply across a range of temperatures, as tends to be required in geological applications.

In this paper, we review experimental data from the literature and use it to derive equation of state parameters and internally consistent values of the enthalpies for pyrite, troilite, a $Fe_{0.875}S$ end-member, named trov, H_2S, S_2, orthorhombic S and anhydrite. The term trov refers only to the $Fe_{0.875}S$ end-member; the term pyrrhotite is used to describe minerals with compositions that fall in the solid solution between FeS and more sulphur-rich compositions. This strategy is employed because it is necessary to be able to distinguish the end-member (trov) from the general solid solution (pyrrhotite). Phase changes are reproduced by a Landau tricritical model (e.g. Holland & Powell, 1990) and a phase change in end-member FeS at 147 °C. Non-ideal mixing in pyrrhotite is dealt with by a combination of a symmetric formalism model (Holland & Powell, 1996) and the use of a hypothetical FeS phase. The hypothetical end-member is necessary to deal with irregularities in ordering in Fe-rich pyrrhotite compositions.

The equation of state of sulphur-bearing fluid end-members is based on a corresponding states approach combined with a compensated-Redlich–Kwong (CORK) equation of state (e.g. Holland & Powell, 1991). Non-ideal mixing in these fluids is described with an asymmetric van Laar formulation (Holland & Powell, 2003). Internally consistent thermodynamic data for the S-bearing phases is added to the data set of Holland & Powell (1998); update 5.5, 22 November 2003), and the program THERMOCALC is used to calculate pseudosections (e.g. Powell *et al.*, 1998), which are phase diagrams for specific rock bulk compositions, for metabasic rocks in the system NCKFMASCOSH (Na_2O–CaO–K_2O–FeO–MgO–Al_2O_3–SiO_2–CO_2–O–S–H_2O). The results are used to draw conclusions on the development of silicate, oxide and sulphide minerals in mafic greenschist facies rocks during metamorphic fluid flow of the type implicated in the formation of greenstone-hosted gold deposits such as those found at Kalgoorlie, Western Australia.

METHODS

Data sources

Data from the literature were critically reviewed and experiments with sufficient information for calculation of enthalpies of reaction were included in a least squares regression (Powell & Holland, 1993) to derive enthalpies for the sulphur-bearing end-member phases. Uncertainties for the compositional data were taken from the published values, or estimated where values were not provided. Experiments included in the fitting exercise are summarized briefly here.

Alcock & Richardson (1951) measured H_2S:H_2 ratios for the iron–troilite–gas assemblage between 447 and 985 °C and at pressures that were unspecified but unlikely to be much different from 1 bar. Radioactive sulphur was used to enable measurement of the gas ratio, and this allowed continuous monitoring of gas ratios and the approach to equilibrium.

Rosenqvist (1954) used a combination of density measurements and direct analysis of a H_2–H_2S gas mixture in equilibrium with troilite and iron to calculate H_2:H_2S ratios for this system. Temperatures were between 400 and 900 °C and pressures were close to 1 bar. These workers also recorded data for pyrite–pyrrhotite and pyrrhotite–iron sulphide liquid systems, but pyrrhotite compositions were not recorded; so, data for the pyrrhotite-bearing experiments were not included in the regression.

Toulmin & Barton (1964) used the electrum tarnish method (Barton & Toulmin, 1964) to determine the fugacity of S_2 gas in equilibrium with pyrrhotite and pyrrhotite–pyrite mixtures. Pyrrhotite compositions were determined by X-ray diffraction. S_2 was assumed to be the predominant sulphur-bearing gas phase at the experimental conditions. Pressures were less than 1 bar except for a few runs at the highest temperatures. Temperature ranged from 300 to 900 °C.

Schneeberg (1973) used electrochemical techniques to measure the fugacity of S_2 buffered by a pyrite–pyrrhotite charge. The cell used contained Ag–AgI–AgS_{2+x} + S_2. Pyrrhotite compositions were determined using XRD following the Yund & Hall (1970) calibration. Pressures were less than 1 bar, and temperatures were between 324 and 438 °C.

Rau (1976) used a combination of indirect sulphur fugacity measurements, where sulphur fugacity was calculated from measurements of the ratio of H_2:H_2S in gases equilibrated with pyrrhotite, and direct measurement, where the sulphur pressure produced by degassing pyrrhotite was measured manometrically. Changes in pyrrhotite composition were calculated from the measured sulphur that was released into the gas phase. There were some difficulties with the assessment of the initial pyrrhotite compositions; so, the absolute pyrrhotite compositions are somewhat uncertain, although relative changes in composition were shown to be reliable by reversal of the experiments. Uncertainty in S fugacities for the indirect measurements were not presented. Pressures for the indirect measurements were mostly less than 1 bar; pressures for the direct measurements were up to 150 bar. Temperatures investigated were between 547 and 1101 °C.

Lin *et al.* (1977) monitored the mass of a sulphide sample that was equilibrated with a metered mixture of H_2 and H_2S gas. Pyrrhotite compositions were calculated from the mass changes. Pressure was unspecified but is unlikely to have been much different from 1 bar. The temperature was 800 °C.

Cemic & Kleppa (1988) determined the enthalpies of formation of pyrite and troilite from their component elements in a twin calorimeter at temperatures between 427 and 748 °C. Pressure was 1 bar. Values for the enthalpy of anyhydrite were taken from the calorimetric determination reported by Majzlan *et al.* (2002).

Heat capacity and enthalpy for troilite and pyrrhotite

Calculation of heat capacity and enthalpy for pyrrhotite is made complicated by a variety of different crystal structures at temperatures less than 325 °C and the existence of multiple phase transitions between 147 and 400 °C (Coughlin, 1950; Grønvold *et al.*, 1991; Grønvold & Stølen, 1992; Fig. 1a–e). Literature data on heat capacity are available for compositions FeS (Coughlin, 1950; Grønvold *et al.*, 1959; Grønvold & Stølen, 1992), $Fe_{0.89}S$ and $Fe_{0.98}S$ (Grønvold & Stølen, 1992), $Fe_{0.9}S$ (Grønvold *et al.*, 1991) and $Fe_{0.875}S$ (Grønvold & Stølen, 1992).

All compositions examined undergo a relatively well-defined phase transition at 325 °C. This transition is attributed to the disordering of antiferromagnetically aligned spins with increasing temperature (Grønvold & Stølen, 1992). Troilite also undergoes multiple phase transitions at around 150 °C (Fig. 1a), which is referred to subsequently as the composite phase transition. These transitions are attributed to structural and magnetic ordering changes (Grønvold & Stølen, 1992). Intermediate pyrrhotite examined also exhibits a composite phase transition at temperatures that increase with an increasing S:Fe ratio. The magnitude of the enthalpy of the composite transition decreases as the S:Fe ratio increases (Fig. 1a–e). The composition $Fe_{0.875}S$ may not record the composite phase transition at all; the region of increased C_p around 430 to 530 °C is thought to involve the dissolution of pyrite in pyrrhotite (Grønvold & Stølen, 1992). The kinetics of this latter reaction are thought to be slow; so, the heat capacity of sulphur-rich pyrrhotite is poorly constrained.

Thermodynamic representation of this complex state of affairs was achieved by the use of two end-members to represent troilite above and below the composite phase transition. The low-temperature end-member is referred to as lot, and the higher temperature end-member as tro. These names are arbitrary and have no history of use with respect to Fe–S phases, so far as the authors are aware. This is a deliberate attempt to reduce nomenclature-related confusion. The composite phase transition is represented by a Landau tricritical transition for lot at 417 K and the 325 °C phase transition is represented by a Landau tricritical transition for tro. The transitions are superimposed on a baseline of the form $C_p = a + bT + cT^{-2}$, the coefficients of which were derived by a fit to the heat capacity data of Grønvold & Stølen (1992). Data points affected by phase transitions were removed and replaced by padding data to facilitate acquisition of the baseline parameters. Identical coefficients were found to be appropriate for both the lot and tro end-members. The S-rich end-member of the pyrrhotite solid solution is represented by an end-member with the formula $Fe_{0.875}S$, which is referred to as trov. Heat capacity for intermediate pyrrhotite was calculated by a simple linear combination between the properties of tro and trov, with the proportion of trov calculated from the formula via $p_{trov} = 8y$ and $p_{tro} = 1 - 8y$, where y is defined by the pyrrhotite formula of $Fe_{1-y}S$. Pyrrhotite compositions with y values greater than 0.125 will have a negative p_{tro}; this is simply a consequence of the choice of end-members and is mathematically and thermodynamically valid.

Tro and lot have identical properties except for the standard state enthalpy and entropy at 25 °C, H^{θ}_{298} and S^{θ}_{298} respectively. H^{θ}_{298} for tro was obtained by minimization of the least squares fit of the experimental data, as described below, while that for lot was

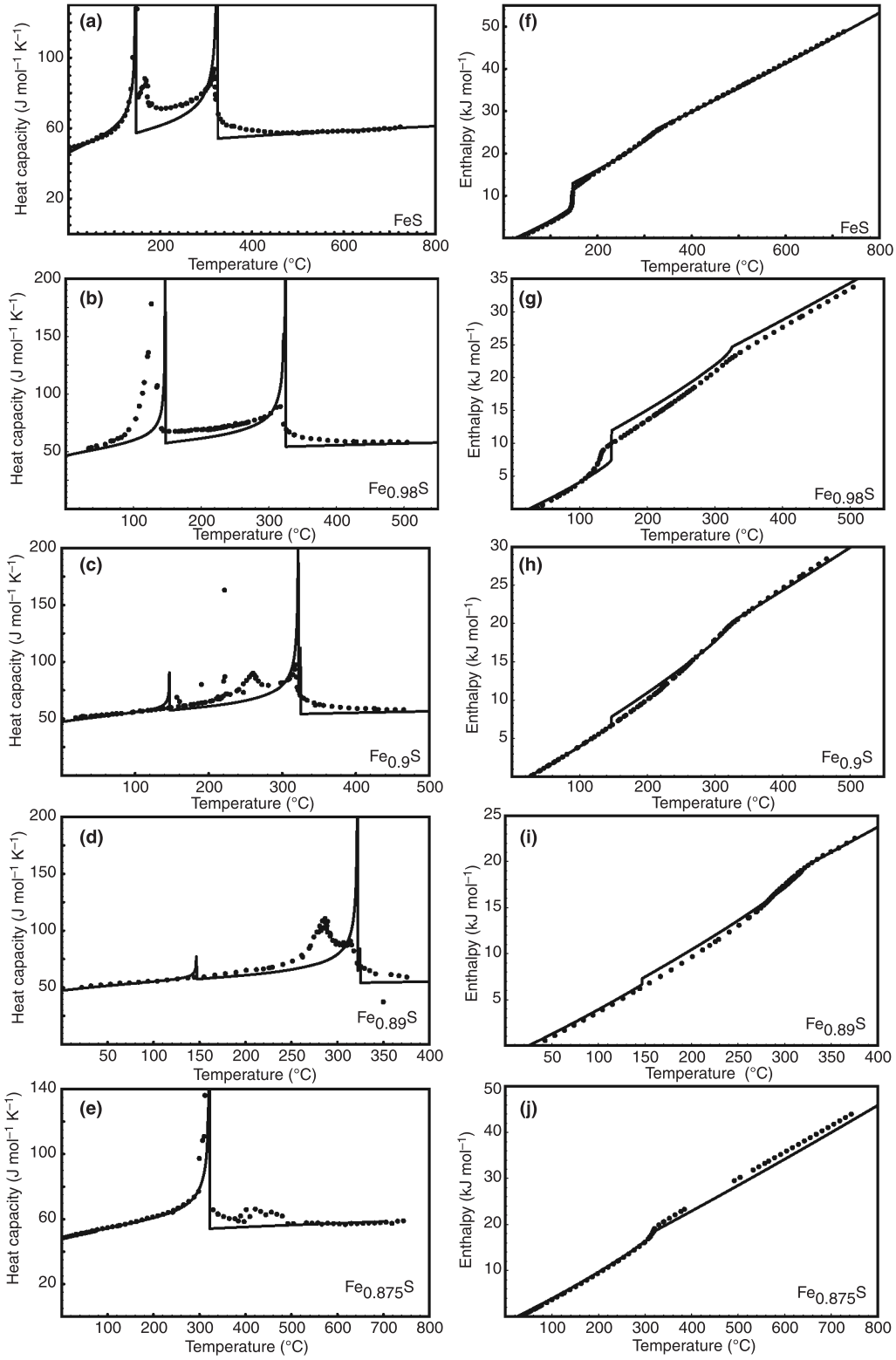

Fig. 1. Comparison of measured and calculated heat capacities and enthalpies for pyrrhotite. Solid lines are calculated fit, dots are data points from Grønvold *et al.* (1991) and Grønvold & Stølen (1992). (a) Heat capacity for FeS; (b) heat capacity for $Fe_{0.98}S$; (c) heat capacity for $Fe_{0.9}S$; (d) heat capacity for $Fe_{0.89}S$; (e) heat capacity for $Fe_{0.875}S$; (f) enthalpy for FeS; (g) enthalpy for $Fe_{0.98}S$; (h) enthalpy for $Fe_{0.9}S$; (i) enthalpy for $Fe_{0.89}S$; (j) enthalpy for $Fe_{0.875}S$.

calculated by subtraction of the integrated enthalpy of the low-temperature transitions from that of the tro. It was necessary to follow this strategy because of the lack of experimental data below 150 °C. The entropy of lot was calculated such that equilibrium between lot and tro was reached at 144 °C, which is the observed temperature of the most intense enthalpy increase (Fig. 1a). The entropy of lot is less than the entropy for tro by 10.8 J mol^{-1} K^{-1}, which is about two-thirds of the entropy involved in the lot–tro phase transition, if the phase transition is assumed to be described by a Landau tricritical model. The additional entropy is likely to be accounted for by features of the transition that are not described by the model, such as changes in entropy due to magnetic ordering. It is unlikely that users of THERMOCALC will utilize the lot end-member to any great extent because tro is the recommended end-member above 150 °C, but its inclusion greatly improves the fit of the heat capacity and enthalpy data to the experimental data (Fig 1a,f). Subsequent references to troilite in the text refer to tro, the high troilite end-member unless lot is specified.

The thermodynamics of Landau transitions are described in detail by Holland & Powell (1992). Briefly, the transition is described by three parameters, T_c, the critical temperature, S_{max}, the maximum entropy of the transition, and V_{max}, which is equal to $S_{max}\,dT_c/dP$. At temperatures less than T_c,

$$C_{p,ex} = \frac{TS_{max}}{2\sqrt{T_c}}(T_c - T)^{-1/2} \quad (1)$$

$$S_{ex} = S_{max}(1 - Q^2) \quad (2)$$

$$H_{ex} = 2S_{max}T_c\left(\frac{Q^6}{6} - \frac{Q^2}{2} + \frac{1}{3}\right), \quad (3)$$

and

$$V_{ex} = V_{max}(1 - Q^2) \quad (4)$$

where

$$Q = \left(1 - \frac{T}{T_c}\right)^{1/4}. \quad (5)$$

At $T > T_c$, $S_{ex}=S_{max}$, $H_{ex} = \frac{2}{3}S_{max}T_c$, $V_{ex}=V_{max}$ and $Q=0$. H_{ex}, S_{ex} and V_{ex} are the excess entropy, enthalpy and volume, respectively, due to the disorder related to the transition at the temperature of interest, and Q is a macroscopic order parameter. T_c was defined to be 325 °C for tro, and 322 °C for trov, on the basis of the heat capacity plots. Initial guesses for S_{max} were taken from integrals of the areas under the heat capacity phase transition peaks. Values for S_{max} were then refined via the least squares fitting process. The best fit values were 10 J mol^{-1} K^{-1} for lot, 12 J mol^{-1} K^{-1} for tro and 10 J mol^{-1} K^{-1} for trov. Values for V_{max} cannot be constrained from the 1-bar heat capacity data and are discussed below.

This strategy replicates heat capacities for troilite and $Fe_{0.875}S$ well at temperatures above the phase transition, and adequately below and at the phase transitions (Fig. 1). Enthalpies are reproduced well for tro, and are slightly underpredicted for trov (Fig. 1j). Higher values of S_{max} could have been used to remove this underprediction, but this was not performed because the lower value of S_{max} replicates the experimental heat capacities at the phase change well, and because heat capacities and enthalpies at temperatures above the phase change are probably slightly overestimated due to dissolution of pyrite in the pyrrhotite phase (Grønvold & Stølen, 1992).

The measured heat capacities and enthalpies of the intermediate pyrrhotites, $Fe_{0.98}S$, $Fe_{0.89}S$ and $Fe_{0.90}S$, for which data are not incorporated in the fit, provide a stringent test of the model. Heat capacities are reproduced approximately for all three intermediate compositions (Fig. 1b–d). Enthalpies are reproduced well for $Fe_{0.89}S$, and for $Fe_{0.90}S$ (Fig. 1h,i), which supports the retention of the lower value of S_{max} for trov. However, enthalpies are predicted less well for the $Fe_{0.98}S$ composition (Fig. 1g). This is attributed to heat capacities for the intermediate phases that are not a linear combination of those of the chosen end-members. These results suggest that there are complex entropic and enthalpic effects that relate to changes in ordering in pyrrhotite, even above the temperature at which the solid solution is thought to be continuous (e.g. Wang & Salveson, 2005). However, these small discrepancies do not prevent good replication of the experimental data by the internally consistent thermodynamic data based on the model assumptions outlined here.

More complex solid solution models were tested in an attempt to improve the agreement between observed and modelled enthalpy example. For example, an order–disorder model (e.g. Holland & Powell, 1996a,b) was applied but failed to improve the fit of the data for the intermediate compositions. However, future versions of THERMOCALC will be able to incorporate multiple order–disorder phase transitions which are more flexible than the tricritical Landau transition, and it is likely that these will enable better representation of the data.

Volume-related parameters

Volume is calculated as described by Holland & Powell (1998).

$$V = V_{PT} + V_{ex} - V_{ex,298} \quad (6)$$

where

$$V_{PT} = V_{1,T}\left(1 - \frac{4P}{\kappa_T + 4P}\right)^{1/4} \quad (7)$$

and

$$V_{1,T} = V_0(1 + a^o(T - 298) - 20a^o(\sqrt{T} - \sqrt{298})), \quad (8)$$

and

$$V_{ex,298} = V_{max}(1 - Q_{298}^2). \quad (9)$$

V_{ex} and Q^2 are defined by Eqns 4 and 5 respectively. κ_T is $\kappa_{298}(1-1.5\times10^{-4}(T-298))$. V_0 was taken from literature compilations or fit to experimental data (Table 3), and expansion and compression coefficients were calibrated against the data listed in Table 3. Values for V_{max} were calibrated mostly against the data of Tenailleau *et al.* (2005) (Fig. 2) because their data were much less scattered than that of Selivanov *et al.* (2003). Calibrated values are consistent with the gradient of the FeS(IV) to FeS(V) phase transition in pressure–temperature space that was measured by Urakawa *et al.* (2004).

Activity–composition relationships for pyrrhotite

Phase relations in the system Fe–S are complex and have been summarized by a number of authors (e.g. Kissin & Scott, 1982; Barker & Parks, 1986; Wang & Salveson, 2005). The bulk of the complexity occurs below 325 °C, and is not considered further here. At the temperatures of interest (325 °C to sulphide melting at 742 to 1188 °C), most pyrrhotite occurs as the 1C hexagonal NiAs structure (Fig. 3). Non-stoichiometric deficiencies in Fe are mostly accommodated by vacancies on Fe sites (e.g. Barker & Parks, 1986), sulphur is five-six co-ordinated (Skinner *et al.*, 2004), and charge balance is maintained by the formation of Fe(III) (Pratt *et al.*, 1994). In the Fe-rich regions ($y < 0.025$), there is evidence for Fe over and above that on the Fe sites, which may be interstitial, or substitute for S (Barker & Parks, 1986; Skinner *et al.*, 2004), but current evidence is ambiguous. Powell (1983) suggested a change in the energetics of substitution at y equal to 0.125, on the basis of the data of Rau (1976) and Burgmann *et al.* (1968), but the proposed discontinuity has also been attributed to the inclusion of metastable microdomains of monoclinic pyrrhotite in the S-rich experiments (Barker & Parks, 1986). Melting begins at 949 °C for pure troilite, and the maximum temperature of stability for pyrrhotite is 1188 °C (Wang & Salveson, 2005).

Here, the pyrrhotite solid solution will be considered to extend from the pure FeS composition through trov, $Fe_{0.875}S$, to more sulphur-rich compositions. The properties of end-member $Fe_{0.875}S$ (trov) were obtained as described above. The optimal FeS end-member for the simple mixing model preferred here does not have exactly the same thermodynamic properties as tro, because of complexities in structure in the Fe-rich pyrrhotite compositions, which introduce

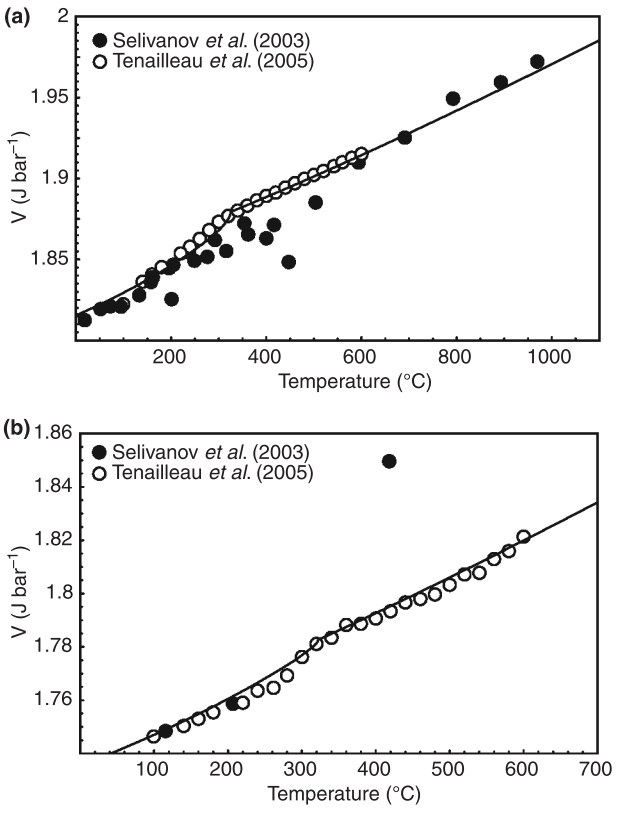

Fig. 2. Measured and calculated volumes for FeS and $Fe_{0.875}S$. Line is calculated volume. (a) FeS; (b) $Fe_{0.875}S$.

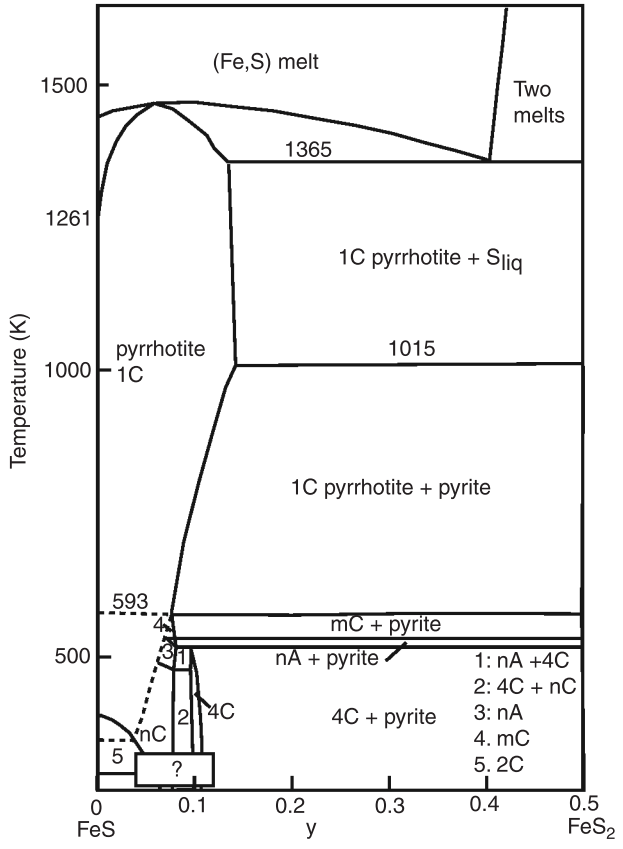

Fig. 3. Phase relations in Fe–S, after Cemic & Kleppa (1988).

irregularities into the properties of compositions with $y < 0.025$ (e.g. Rau, 1976). For this reason, we allow the FeS end-member in pyrrhotite to be hypothetical. The hypothetical end-member is named trot. This phase has the same heat capacity and phase transition characteristics as tro, the real troilite end-member, but the enthalpy and entropy are allowed to vary to optimize the fit between experiment and the model. If such an end-member were not necessary then the properties of tro and trot would be identical, within error; so, the fitting process acts as a test for the need of the hypothetical trot end-member.

The data of Rau (1976) were used to calibrate the regular solution activity–composition model (e.g. Holland & Powell, 1996b) for mixing between trot (FeS) and trov ($Fe_{0.875}S$). Data for the most iron-rich compositions ($y < 0.025$) could not be reproduced by the model, even when using the trot end-member, and were removed from the fitting data set. The discrepancy is attributed to irregularities in Fe ordering in the most Fe-rich compositions so that the most iron-rich compositions behave like tro instead of trov. For this reason, model results should be interpreted with caution when pyrrhotite compositions more iron-rich than $Fe_{0.98}S$ are predicted.

The equilibrium used for calibration is

$$8Fe_{0.875}S(trov) = 7FeS(trot) + \frac{1}{2}S_2, \qquad (10)$$

for which

$$\Delta G = 0 = \Delta G^{\theta} + RT\ln\frac{a_{trot}^{7} f_{S_2}^{\frac{1}{2}}}{a_{trov}^{8}} \qquad (11)$$

which is equal to

$$\Delta G = 0 = \Delta G^{\theta} + RT\ln\frac{a_{trot,id}^{7} f_{S_2}^{\frac{1}{2}}}{a_{trov,id}^{8}} + 7RT\ln\gamma_{trot} - 8RT\ln\gamma_{trov} \qquad (12)$$

The activity terms are dealt with by a symmetric formalism model, so

$$RT\ln\gamma_{trot} = (1 - p_{trot})^2 w_{trot-trov} \qquad (13)$$

and

$$RT\ln\gamma_{trov} = p_{trot}^2 w_{trot-trov} \qquad (14)$$

p_{trot} is defined by

$$p_{trot} = 1 - 8y \qquad (15)$$

where y is defined by the pyrrhotite formula $Fe_{1-y}S$. Ideal activities are described by a mixing-on-sites expression, where Fe is allowed to mix across the whole site. Under this assumption,

$$a_{trot,id} = x_{Fe} = 1 - y \qquad (16)$$

and

$$a_{trov,id} = c x_{Fe}^{\frac{7}{8}} x_{V}^{\frac{1}{8}} = c(1-y)^{\frac{7}{8}} y^{\frac{1}{8}} \qquad (17)$$

where x_V is the proportion of vacancies on the Fe site and c is a normalization constant. The value of c is 1.4576. Substitution of Eqns 13–17 into Eqn 12 gives

$$\Delta G = 0 = \Delta G^{\theta} + RT\ln\frac{f_{S_2}^{\frac{1}{2}}}{cy} + w_{trot-trov}(7p_{trov}^2 - 8p_{trot}^2). \qquad (18)$$

which can be arranged to produce the equation of a straight line, with $RT\ln(f_{S_2}^{\frac{1}{2}}/cy)$ as the y coordinate, $(7p_{trov}^2 - 8p_{trot}^2)$ as the x coordinate, and $w_{trot-trov}$ as the gradient.

This method was applied to the data of Rau (1976). Pyrrhotite composition data for experiments where sulphur fugacities were measured indirectly, and were thus subject to possible systematic error, as discussed by Rau (1976), were adjusted by $-0.003(1 - y)$ as suggested by Powell (1983). The remainder of the data at temperatures between 547 and 1101 °C were fit to the model simultaneously to produce a single value for $w_{trot-trov}$, of -3.19 ± 0.04 kJ mol^{-1} (Fig. 4a). Alternative models that utilize van Laar asymmetric formalism (Holland & Powell, 2003), different end-member choices and mixing models that involved mixing across only a fraction of the available site, were also applied to the data, but the simple regular solution model performed as well or better than any of the more complicated models and is therefore preferred.

Fluid end-member properties and activity composition relationships

Fluid end-members considered are the pure fluids, H_2S and S_2, and the aqueous species HS^-, HSO_3^-, SO_4^{2-} and HSO_4^-. Entropies for H_2S and S_2 are taken from Cox *et al.* (1987), and heat capacities from data tabulated by Chase (1998). Data for the aqueous sulphur-bearing

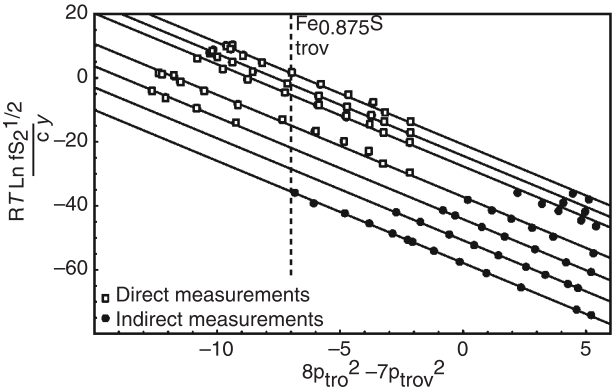

Fig. 4. Comparison of calculated and measured activity–composition parameters for a $w_{trot-trov}$ of -3.19 kJ mol^{-1}. Data points acquired by the indirect method are shifted by $0.003(1 - y)$ as suggested by Powell (1983). y is defined by the pyrrhotite formula $Fe_{1-y}S$. Data from Rau (1976).

species are from Shock & Helgeson (1988); enthalpies for these phases are fixed to those from the literature and are not optimized during the least squares fitting process because of the lack of experimental data at the pressures and temperatures of interest.

Mixing of pure fluid end-members is accounted for by the van Laar asymmetric formalism (VL-ASF) approach (Holland & Powell, 2003), and for the aqueous species by the Debye–Huckel asymmetric formalism (DH-ASF) (Evans & Powell, 2006). These methods are fully compatible and allow mixing between aqueous and fluid phases in mixed solvents and high ionic strength solutions to be considered. ASF parameters for the aqueous species were set to zero, for want of sufficient experimental data at the pressures and temperatures of interest to warrant further calibration. ASF parameters to describe mixing between the pure fluids H_2S and H_2O were calculated by a fit of the VL-ASF expression for activity coefficients to the modified Redlich–Kwong expression (Holloway, 1977; Flowers, 1979), with Redlich–Kwong parameters calculated by a corresponding states approach (Holloway, 1977). A value for $a_{H_2S-H_2O}$ of 6.5 kJ mol^{-1} was found to fit the Redlich–Kwong expression over a range of pressure and temperature (Fig. 5a). Values for $a_{H_2S-CH_4}$ and $a_{H_2S-CO_2}$ of 4.15 kJ mol^{-1} (Fig. 5b) and 0.045 kJ mol^{-1} (Fig. 5c), respectively, were calculated by the same method. Values were optimized at 0.4 GPa and 600 °C. S_2 gas was considered to mix ideally as it tends not to be present in significant concentrations in geological environments; however, it was included in the database to aid testing of the database against experimental data.

Derivation of enthalpies

An internally consistent set of enthalpies for the solid and fluid end-members (Tables 1 & 2) was derived by the weighted least squares minimization method described by Powell & Holland (1985) and Powell & Holland (1993). Inputs were the enthalpies of reaction for the equilibrium or equilibria associated with each of the data points in each of the listed experiments at reference state conditions (25 °C and 1 bar). The enthalpies were calculated from the reported experimental parameters and specified entropies, volumes, heat capacities, thermal expansions and compressibilities, and activity–composition models. Data sources for the set thermodynamic parameters are discussed above, and summarized in Table 3. Solute aqueous end-members were not included in the least squares minimization, because of a lack of well-constrained experimental data at the pressures and temperatures of interest.

Initial estimates of the reference state enthalpies for the solid and pure fluid end-members were refined and optimized by least squares minimization of the residuals between the fit and calculated average enthalpy for each experimental data set. Uncertainties and correlations between the fit enthalpies were also calculated, which facilitates error propagation on thermodynamic calculations made using the data set. Uncertainties on the final enthalpies are based on input estimates of experimental uncertainties and the spread of the experimental data. Literature estimates of experimental uncertainties were absent in some cases, and less than would be expected if the full range of contributions to uncertainty had been taken into account in others. In these cases the experimental uncertainties were estimated.

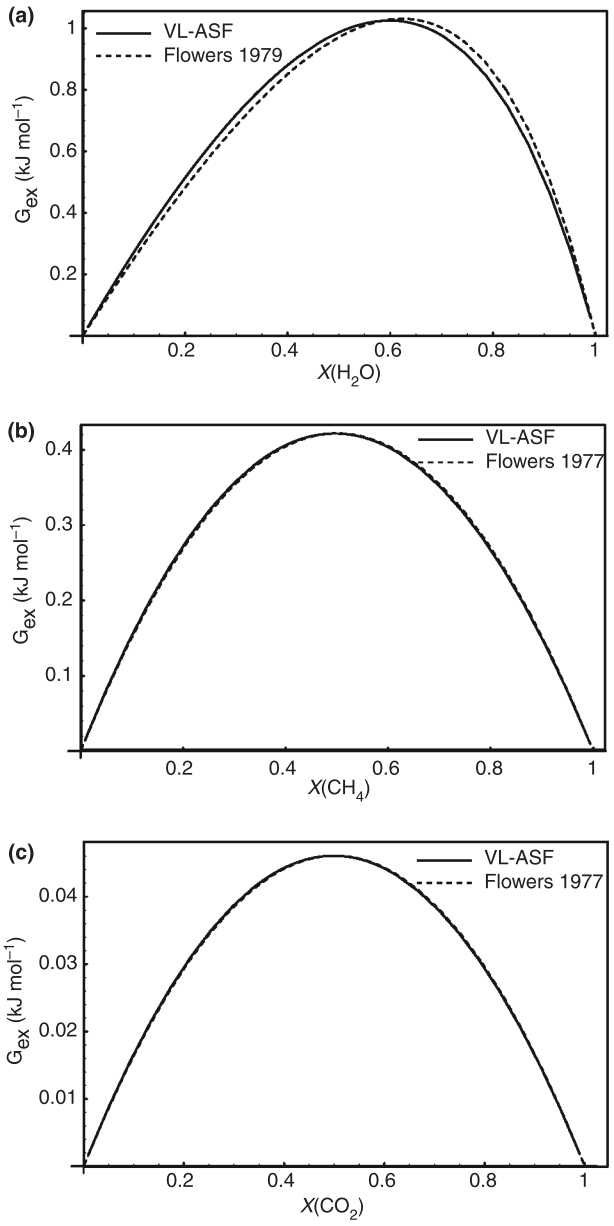

Fig. 5. Comparison of calculated mixing relations for H_2S-bearing fluids with excess Gibbs free energy calculated with the VL-ASF equations (Holland & Powell, 2003) and the modified Redlich–Kwong approach (Flowers, 1979) at 0.4 GPa and 600 °C. (a) H_2S–H_2O; (b) H_2S–CH_4; (c) H_2S–CO_2.

Table 1. Thermodynamic data for mineral and fluid end-members.

	pyr	tro	trot	lot	trov	any	S_2	H_2S
$\Delta H^0_{f,298}$ (kJ mol^{-1})	−171.73	−97.99	−99.03	−102.4	−96.05	−1433.8	128.34	−20.28
$\sigma(\Delta H^0_{f,298})$ (kJ mol^{-1})	0.25	0.07	0.17	0.07	0.15	1.35	0.27	0.1
S (J mol^{-1} K^{-1})	52.9	70.8	65.5	60	57.5	106.9	231	205.77
V (J bar^{-1})	2.394	1.819	1.819	1.818	1.738	4.594	0	0
$C_{p,a}$ (kJ mol^{-1} K^{-1})	0.0373	0.0502	0.0502	0.0502	0.0511	0.1287	0.0371	0.0474
$C_{p,b} \times 10^5$ (kJ mol^{-1} K^{-2})	2.6715	1.1052	1.1052	1.1052	0.8307	4.8545	0.2398	1.024
$C_{p,c}$ (kJ mol^{-1} K)	−1817	−940	−940	−940	−669.7	−1223	−161	615.9
$C_{p,d}$ (kJ mol^{-1} K$^{-1/2}$)	0.6492	0	0	0	0	−0.5605	−0.065	−0.3978
$a^o \times 10^{-5}$(K^{-1})	6.38	11.14	11.14	9.67	12.25	8.43	n.a.	n.a.
κ (GPa)	1.395	0.658	0.658	0.658	0.658	0.544	n.a.	n.a.
T_c (K)	n.a.	598	598	420	595	n.a.	n.a.	n.a.
S_{max} (J mol^{-1} K^{-1})	n.a.	12	12	10	10	n.a.	n.a.	n.a.
V_{max} (J bar^{-1})	n.a.	0.041	0.041	0	0.016	n.a.	n.a.	n.a.

Table 2. Thermodynamic data for solute end-members.

	HS^-	HSO_3^-	SO_4^{2-}	HSO_4^-
$\Delta H^0_{f,298}$ (kJ mol^{-1})	−16.04	−623.82	−906.12	−885.7
$\sigma(\Delta H^0_{f,298})$ (kJ mol^{-1})	5.15	5.15	5.15	5.15
S (J mol^{-1} K^{-1})	68	139	18.8	125.04
V (J bar^{-1})	2.065	3.33	1.388	3.52
$C_{p,298}$ (kJ mol^{-1} K^{-1})	−0.092	−0.0058	0.268	0.022

Table 3. Sources of data for mineral and fluid end-members.

	Pyrite	tro, trot	lot	trov	any	S_2	H_2S
S	1	6	6	6	10	14	14
$C_{p,a-d}$	2	6	6	6	11	2	2
V	3	7	7	7	3		
a^o	4	7	8	7	12		
κ	5	9	9	9	13		
T_c		6	6	6			
S_{max}		6	6	6			
V_{max}		7		7			

1 = Chase (1998); 2 = fit to equation which is derived from fits to data tabulated in Chase (1998); 3 = Robie (1966); 4 = fit to data in Skinner (1966); 5 = fit to data in Adams & Williamson (1923); 6 = optimized, see text; 7 = fit to data from Tenailleau *et al.* (2005); 8 = fit to data in Taylor (1970); 9 = fit to data for troilite in King & Prewitt (1982); 10 = Robie & Hemingway (1995); 11 = fit to expression in Majzlan *et al.* (2002); 12 = fit to data in Evans (1979); 13 = from data in Birch (1966); 14 = Cox *et al.* (1987).

Experimental data for the sulphur-bearing minerals considered here do not include other end-members considered in the data set except for elemental Fe and H_2 gas; so, the data set is effectively independent of the S-free end-members. Fit diagnostics provided (Table 4) are *uH*, a measure of the pressure- and temperature-related uncertainty on the experimental bracket, *d*/*s*, a comparison of experimental bracket width with the uncertainties on bracket ends and *h* a measure of the influence of the equilibria on final calculated enthalpies. *d*/*s* values less than two are acceptable. *h* varies between 0 and 1; low *h* indicates that the final enthalpies are effectively independent of a particular experimental data set and vice versa. Weightings for each data set are also included in Table 4; these are used to indicate the relative reliability of the experiments. A weighting of one indicates maximum reliability. Fit diagnostics for the calorimetry constraints are slightly different to those for the experimental data sets used to derive enthalpy brackets. The diagnostics provided are *h*, which, as before, is a measure of influence of the calorimetric measurement on calculated enthalpies and *e**, which measures the discrepancy between the final least squares enthalpy and the calorimetric measurement. Values for *e** of less than 2.5 are deemed acceptable.

Initial results for the regression showed that enthalpy values close to the initial estimates could be obtained using all the experimental data considered, except those of Alcock & Richardson (1951) and Schneeberg (1973). The Alcock and Richardson data

Table 4. Fit diagnostics.

Source	Equilibria	*uH*	*d*/*s*	*h*	*e**	Within bracket
Grønvold & Stølen (1992)	lot = tro	0.04	1	0.89	n.a.	Yes
Rau (1976)	16 trov = 14 trot + S_2	3.98	-0.2	0.71	n.a.	Yes
Lin *et al.* (1977)	8 trov + H_2 = 7 trot + H_2S	1.92	0.3	0.08	n.a.	Yes
Toulmin & Barton (1964)	16 trov = 14 trot + S_2	3.7	-0.8	0	n.a.	Yes
Toulmin & Barton (1964)	16 trov = 14 trot + S_2	3.37	0.1	0.23	n.a.	Yes
Toulmin & Barton (1964)	2 trot + S_2 = 2 pyr	1.75	-0.7	0.56	n.a.	Yes
Schneeberg (1973)	16 trov = 14 trot + S_2	not used				
Schneeberg (1973)	2 pyr = 2 tro + S_2	not used				
Rosenqvist (1954)	Fe+H_2S=tro+H_2	0.44	-2.3	0.38	n.a.	Yes
Alcock & Richardson (1951)	Fe+H_2S=tro+H_2	not used				
Cemic & Kleppa (1988)	lot = Fe + S	n.a.	n.a.	0.51	-0.2	n.a.
Cemic & Kleppa (1988)	pyr = Fe + 2S	n.a.	n.a.	0.61	0.1	n.a.
Majzlan *et al.* (2002)	Ca+S+2O_2=$CaSO_4$	n.a.	n.a.	1	0	n.a.

set is one of two that explores the iron–troilite–gas equilibria, along with Rosenqvist (1954), and the two data sets are slightly inconsistent with each other. It was possible to fit both simultaneously if the experimental uncertainties were increased; however, it is statistically preferable to exclude one of the data sets. Inclusion of the data set of Rosenqvist (1954) produced values for the enthalpy of H_2S that were closer to published values than those obtained when the Alcock and Richardson data set was included; so, the former was preferred for the final fit (Table 4). Ideally, the data set of Schneeberg (1973) would have been included in the data set, as it provides constraints on the pyrite–pyrrhotite equilibrium at relatively low temperatures (324–438 °C), and is generally consistent with the rest of the data. However, there are only four data points, and, while these were almost in agreement with the other data, there were small discrepancies (2–8 °C) in excess of the stated uncertainties; so, the data were excluded. The benefit of the exclusion is that the Schneeberg data may be used as a test for the final data set.

The data of Toulmin & Barton (1964) were also slightly in disagreement with those of Rau (1976), although the combined experimental bracket for each data set was within that expected from the fit enthalpies; so, the discrepancies were small. The Rau data were consistent with those of Burgmann *et al.* (1968), which were used as an independent test of the model (see below), while the Toulmin & Barton (1964) data, which also have much larger uncertainties due to the nature of the experiments, were not.

Calculated σ_{fit} for the regression is 1.031 with 275 degrees of freedom, which compares satisfactorily with values for previous versions of the data set (Holland & Powell, 1990, 1998). Fit values for the end-member reference state enthalpies were compared with those from literature compilations (Table 5) and found to be comparable.

Calculated values for experimental data

A measure of the ability of the final data set to reproduce the input data points is provided by a comparison of calculations with the literature-derived data (Fig. 6). Data from additional studies that were not included in the regression are also shown; these are data for pyrrhotite–gas equilibria from Burgmann *et al.* (1968) (Fig. 6b) and for the pyrite–pyrrhotite equilibria from Arnold (1951) and Schneeberg (1973) (Fig. 6d). Uncertainties used in the figure are those specified by the literature, where available, although in many cases these are smaller than the data points themselves.

The majority of the data points fall acceptably close to the calculated trends. The data of Rau (1976) (Fig. 6a) lie on the calculated lines at all temperatures and across the greater part of the compositional range investigated. Small discrepancies are noted at pyrrhotite compositions close to FeS. This reflects divergence of measured compositions from those predicted by the symmetric formalism activity–composition model at these compositions, as noted above. Pyrrhotite compositions for the pyrrhotite–gas equilibrium experiments of Toulmin & Barton (1964) and Burgmann *et al.* (1968) are predicted very well (Fig. 6b) in spite of the independence of these latter data from the final fit values. The majority of data for the iron–troilite–gas equilibria fall on or within error of the calculated line (Fig. 6c), and the distribution of the data points illustrates the small but systematic difference between the Alcock & Richardson (1951) and Rosenqvist (1954) data sets; THERMOCALC calculations fit the Rosenqvist (1954) data, as would be expected given the inclusion of these data in the regression. Calculated temperatures and pyrrhotite compositions for the pyrite–pyrrhotite equilibrium are close to observed values (Fig. 6d), although the model systematically underpredicts the sulphur content of troilite at temperatures close to pyrite melting. In terms of the model, this is a consequence of optimization of heat capacities for intermediate pyrrhotite compositions rather than for the most sulphur-rich ones.

Table 5. Comparison of derived values for $\Delta H_{f,298}$ with literature values.

Phase	THERMOCALC	C85	B95	RH95	C98	WP05
pyr	−171.7	−171.5		−171.5	−171.5	−171.1
lot	−102.4	−101.7		−102.6	−101.7	−100.1
tro	−99.0					−96.3
trov	−96.1			−97.5	−105.4	−94.4
any	−1433.8		−1434.1			
S_2	128.3	128.6				
H_2S	−20.3				−20.5	

All values are in kJ mol^{-1}. C85 = Chase *et al.* (1985); B95 = Barin (1995); RH95 = Robie & Hemingway (1995); C98 = Chase (1998); WP05 = Waldner & Pelton (2005).

Range of applicability

The data are considered to be applicable over the pressure and temperature range of the experimental data from which the experimental data set is derived, and applicable, with caution at pressures and temperatures outside those conditions. Thus, data for the solid phases can be considered reliable from 300 to 1100 °C. Extension to pressures higher than 1 bar is possible because of single-phase compressibility measurements, which exist for pressures up to 1.2 GPa for pyrite, and from 0.4 to 15 GPa for troilite; however, confirmation of phase boundaries at pressures of geological interest is desirable. The mixing model that allows H_2S to be considered in the fluid phase is more restricted and should be treated with caution at conditions far from the calibration conditions of 0.4 GPa and 600 °C, although experimental data are replicated adequately at 0.1 GPa and 300–500° C.

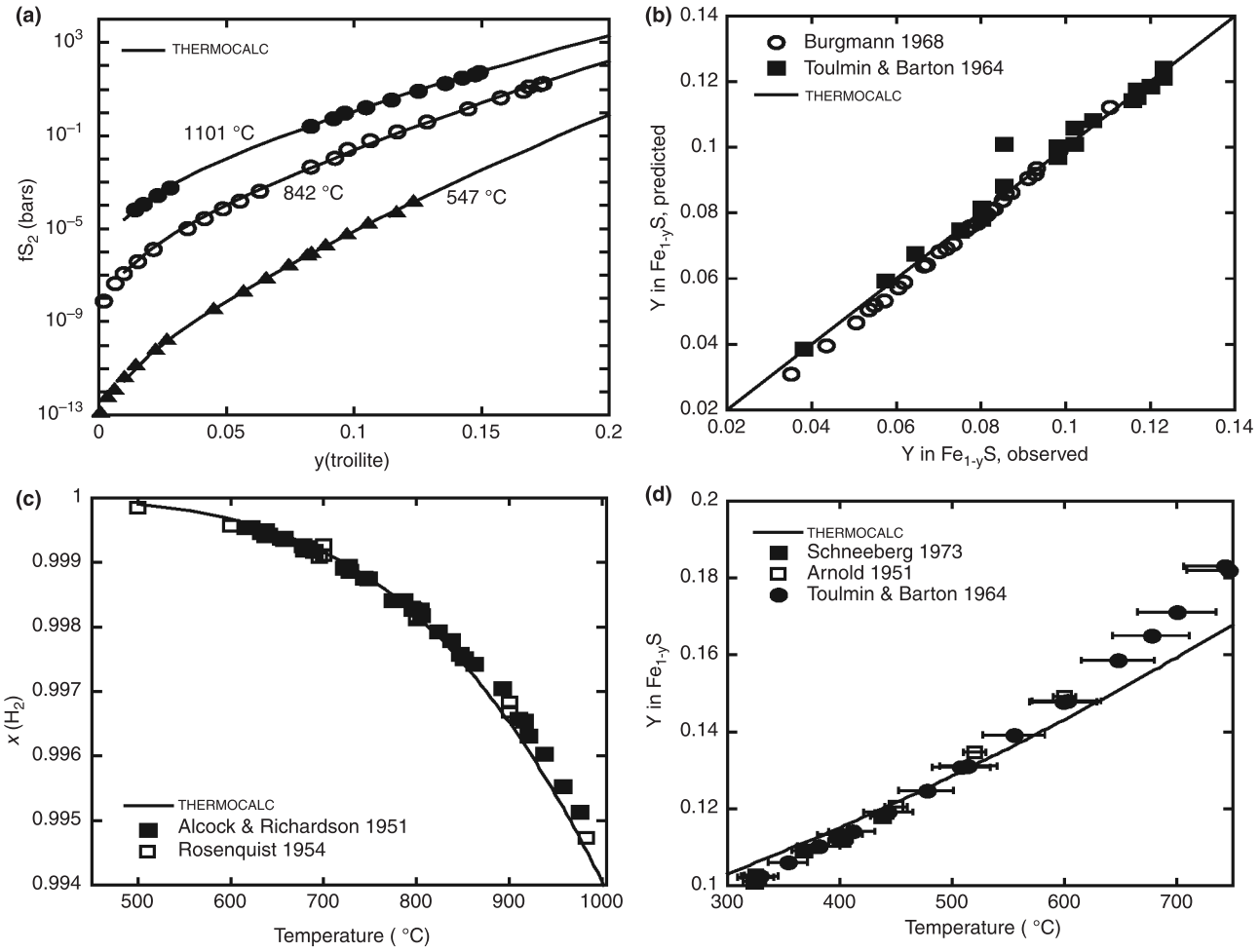

Fig. 6. Comparison of experimental with calculated fluid and mineral compositions. (a) Data for pyrrhotite–sulphur gas equilibria from Rau (1976); (b) pyrrhotite composition data from Toulmin & Barton (1964) and Burgmann *et al.* (1968); (c) data for the troilite–gas equilibria from Alcock & Richardson (1951) and Rosenqvist (1954); (d) temperature–pyrrhotite composition data for the pyrrhotite–pyrite equilibria from Arnold (1951), Toulmin & Barton (1964) and Schneeberg (1973).

Replication of aqueous S-bearing experimental data

Literature reports of experiments on S-bearing aqueous systems at the pressures and temperatures of interest (> 300 °C and 30 MPa) are rare because reliable measurement of solution concentrations at these elevated pressures and temperatures is so difficult. However, Kishima (1989) recorded concentrations of H_2S and H_2 in solution in equilibrium with the pyrite–pyrrhotite–magnetite buffer at 300–500 °C and pressures to 0.1 GPa. These data were not used in the production of the data set, so provide a demanding test of the data and associated activity–composition models. The experimental observations were compared with solubilities calculated by THERMOCALC, and were found to replicate the experiments reasonably well (Fig. 7). Discrepancies are attributed to the experimental pressures which are somewhat lower than those for which the CORK EOS parameters (Holland & Powell, 1991) for these gases are optimized.

APPLICATION TO SULPHIDE-BEARING MINERAL ASSEMBLAGES IN GREENSTONES

Geological background

The sulphur-bearing data set and mineral and fluid activity–composition models described above were used to investigate the development of metamorphic mineral assemblages in greenschist facies metabasalts of the type that host giant Archean gold deposits such as the one at Kalgoorlie in Western Australia (e.g. Phillips, 1986). The stability of S-bearing minerals in such rocks is of interest because S complexes with gold in aqueous solution (e.g. Benning & Seward, 1996); so, changes to the S-bearing mineral assemblage can influence the mobilization, transport and deposition of gold.

Mineral and bulk-rock compositions and petrographic relationships are described in detail by a number of authors (e.g. Phillips, 1986; Boulter *et al.*,

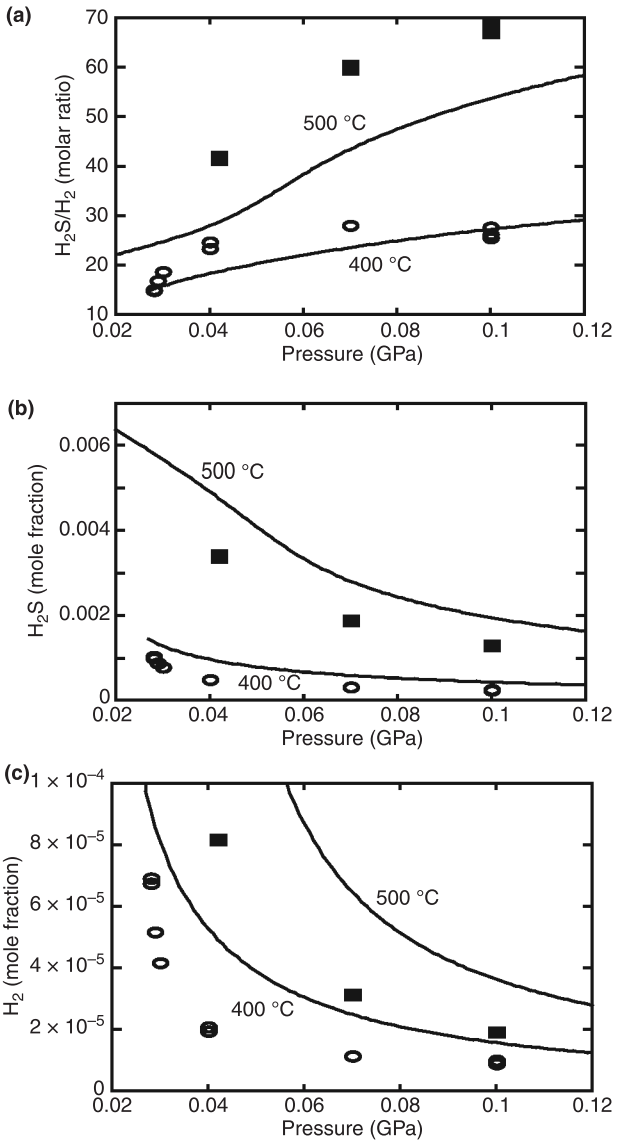

Fig. 7. Comparison of measured and calculated fluid compositions with data from Kishima (1989), which was not used in the least squares minimization. (a) pressure–gas composition relations; (b) pressure–absolute H_2 concentrations; (c) pressure–absolute H_2S relationships.

1987; Phillips & Brown, 1987; Phillips & Gibb, 1993; White *et al.*, 2003; Bateman & Hagemann, 2004) and are only briefly summarized here. Bulk-rock compositions are tholeiitic, with much of the gold hosted by iron-rich, magnetite-bearing lithologies in the Golden Mile Dolerite and Paringa Basalt. The rocks were metamorphosed at greenschist facies conditions prior to mineralization and rocks that show little sign of the carbonation and hydrothermal alteration that accompanies mineralization contain the assemblage actinolite–albite–chlorite–epidote–magnetite ± quartz. Igneous Ti-rich magnetite is commonly altered to leucoxene, ilmenite and pyrite. Mineralization was accompanied by extensive carbonation, sulphidation and hydrothermal alteration. The most distal alteration zone is the chlorite alteration zone, in which the mineral assemblage is chlorite–calcite–dolomite–albite–quartz–magnetite with trace pyrite, and siderite in Fe-rich lithologies. Note that dolomite refers to all minerals of the composition $Ca(FeMg)CO_3$, that is, it covers ankeritic compositions. The intermediate carbonate alteration zone is more intensely carbonated and rocks contain the assemblage dolomite, quartz, albite, ilmenite, magnetite, muscovite, chlorite, pyrite ± siderite ± hematite. The mode of chlorite is generally smaller than that in the less altered distal alteration zone. The most gold-rich alteration in the pyrite-rich proximal zone has a bleached appearance which reflects the partial or complete loss of chlorite, and contains dolomite, albite, pyrite, muscovite, quartz ± chlorite ± siderite ± hematite. Feldspar in all zones is of albitic composition (Phillips & Gibb, 1993). The composition of fluid inclusions in vein quartz indicate that the fluid associated with mineralization was relatively low salinity (< 2 wt% NaCl equivalent) and CO_2-rich, with $X(CO_2)$ between 0.2 and 0.3 (Ho *et al.*, 1992).

Previously, fluid inclusions have been used to estimate the pressure, temperature and bulk compositions that accompanied mineralization (e.g. Ho *et al.*, 1992). Pseudosections, phase diagrams calculated for a specific bulk composition, have also been used to investigate the effects of rock bulk composition, pressure, temperature and fluid composition on the silicate mineral assemblage (White *et al.*, 2003). Mineral assemblages imply equilibration at 315–350 °C and 0.1–0.2 GPa at an $X(CO_2)$ of 0.1–0.25, with more CO_2-rich fluid compositions found in the proximal alteration zones (White *et al.*, 2003).

Pseudosection calculation methods

P–T (Fig. 8), *T*–$X(CO_2)$ (Fig. 9), *T*–*X*(S) (Fig. 10a) and *X*(S)–$X(CO_2)$ (Fig. 10b) pseudosections were calculated using THERMOCALC v3.22 and the Holland & Powell (1998) data set v5.5, updated 22 November 2003 and augmented with the data for the sulphur-bearing end-members presented here (ts-ds55S.txt). The chemical system investigated was NCKFMASCOSH (Na_2O–CaO–K_2O–FeO–MgO–Al_2O_3–SiO_2–CO_2–O–SO_2–H_2O). Phase relations were calculated at pressures ranging from 0.1 to 0.5 GPa and temperatures from 300 to 500 °C. Pseudosections were used because the chemical system investigated is complex; so, high-variance assemblages might be expected, and pseudosections allow the boundaries of high-variance assemblages to be delineated when bulk composition is fixed. Previous work (e.g. Frost, 1979, 1985) has investigated low-variance phase relations in subsystems of NCKFMASCOSH, and the topology of the diagrams presented by these workers forms the underlying structure for the

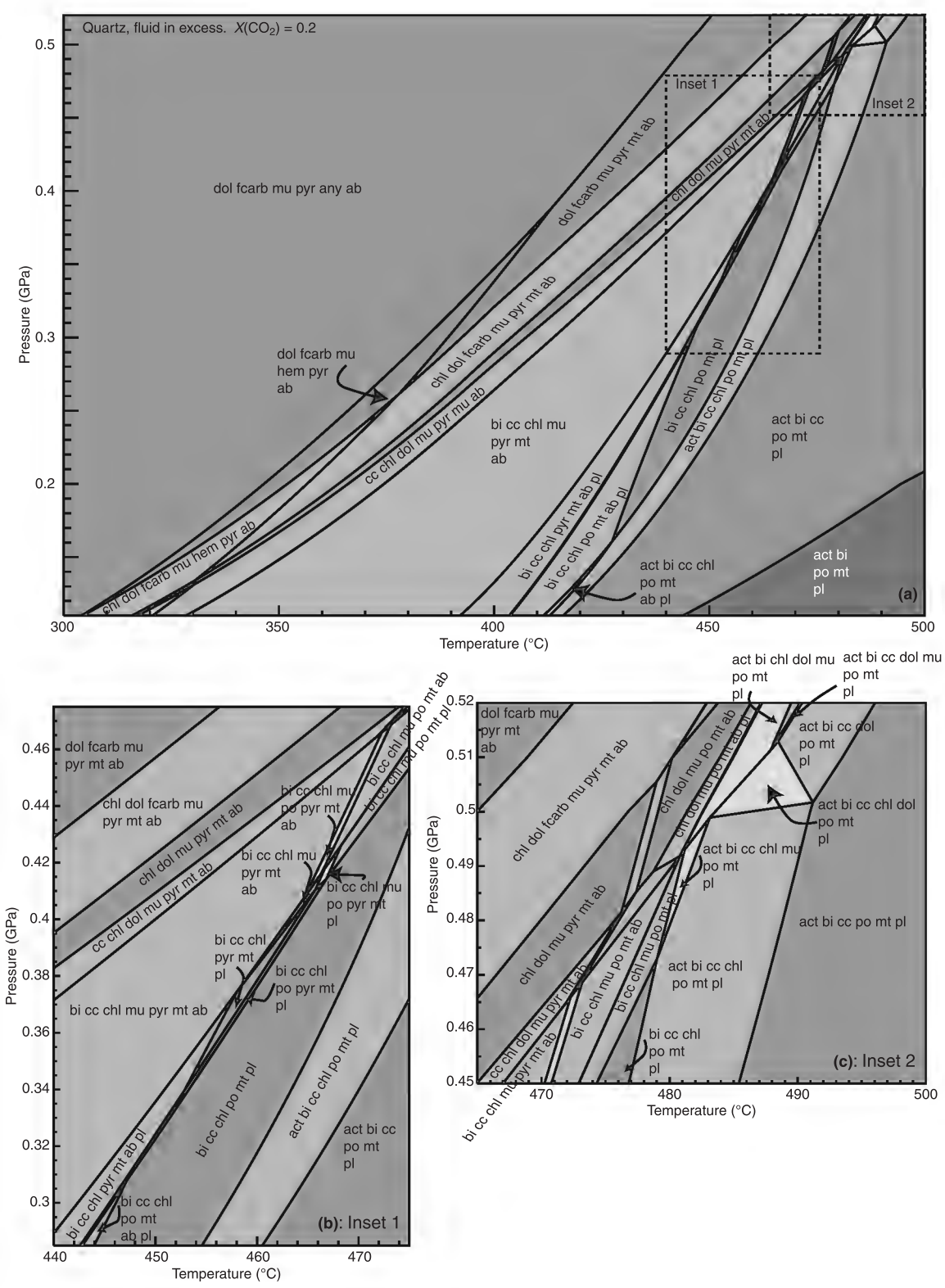

Fig. 8. *P–T* pseudosection for the bulk composition in Table 6 at $X(CO_2)$ of 0.2. Quartz and fluid in excess. (a) Full pseudosection; (b) inset to illustrate the interplay between albite–plagioclase and pyrite–pyrrhotite stabilities; (c) inset to illustrate the divariant field at 0.5 GPa. Abbreviations are ab: albite; act: actinolite; any: anhydrite; bi: biotite; cc: calcite; chl: chlorite; dol: dolomite; mu: muscovite; fcarb: iron carbonate; pl: plagioclase; pyr: pyrite; po: pyrrhotite; hem: hematite; mt: magnetite.

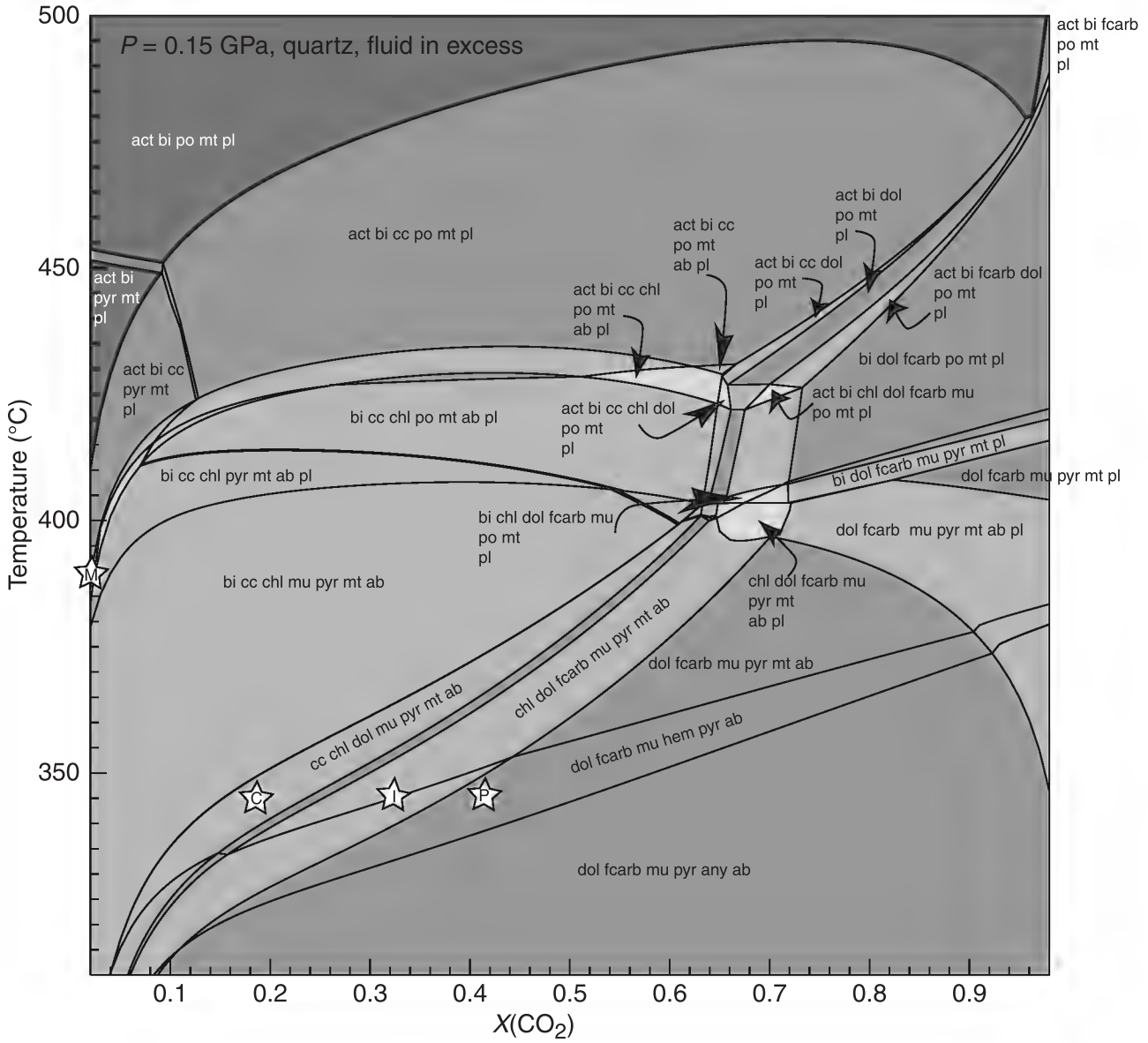

Fig. 9. T–$X(CO_2)$ pseudosection for the bulk composition in Table 6 at 0.15 GPa. Quartz and fluid in excess. Abbreviations as for Fig. 8. Letters in stars relate to assemblages seen in greenschist facies mafic rocks from the Golden Mile, Kalgoorlie. M, prehydrothermal alteration; C, distal alteration; I, intermediate alteration; P, proximal alteration.

sequence of reactions observed in the pseudosections. Such diagrams, while useful, particularly in systems with relatively small numbers of components, show the mineral assemblage as a function of intensive chemical potentials such as oxygen fugacity and hydrogen fugacity. The pseudosection approach provides a useful complement to the chemical potential approach because only the bulk composition, pressure, temperature and, in some cases, fluid composition, needs to be specified.

The bulk composition used (Table 6) is that of a carbonated Golden Mile Dolerite, from the carbonate alteration zone at Kalgoorlie, Western Australia (Phillips, 1986, Table 6, composition 3). Specification of S in the bulk composition for THERMOCALC is as SO_2; so, it is necessary to balance the S with negative quantities of O to produce S in the valence states of interest in pyrite and pyrrhotite, which are −1 and −2 respectively. The proportion of O also determines the quantity of Fe(3+); so, $n(O)=0.5n(Fe^{3+}) - 3n(S^{2-}) - 2.5n(S^{-}) + n(S^{6+})$, where n denotes the number of moles of the species considered. This strategy works well; S in valence +6 (anhydrite), −1 (pyrite) and −2 (pyrrhotite) are predicted in equilibrium with Fe(3+) bearing phases at plausible pressures, temperatures and fluid compositions.

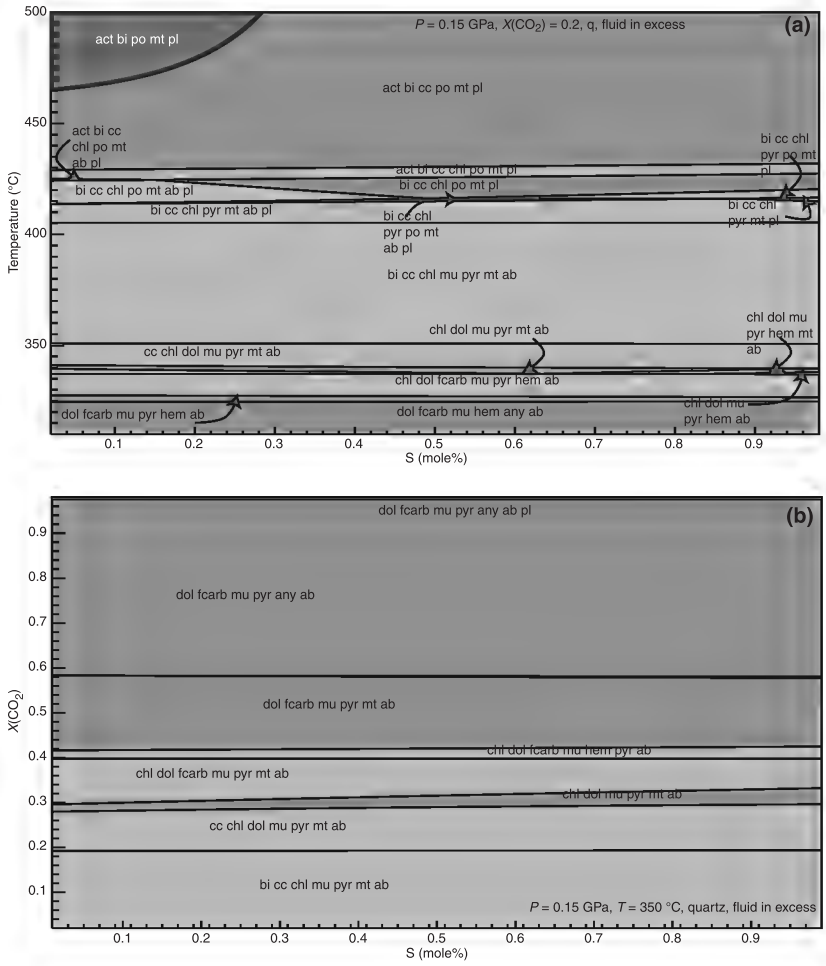

Fig. 10. (a) *T*–*S* pseudosection for the range of bulk compositions in Table 6 at a pressure of 0.15 GPa and an $X(CO_2)$ of 0.2. (b) *S*–$X(CO_2)$ pseudosection for the bulk composition in Table 6 at a pressure of 0.15 GPa and a temperature of 350 °C.

Table 6. Bulk compositions (wt%) used for pseudosection construction.

	SiO_2	Al_2O_3	CaO	MgO	FeO	K_2O	Na_2O	O	SO_2
Figs 8 & 9	52.63	14.63	8.55	4.34	15.14	1.69	2.96	−0.05	0.1
S-rich end-member for Fig. 10	52.41	14.57	8.51	4.32	15.08	1.68	2.95	−0.48	0.95
S-poor end-member for Fig. 10	52.65	14.64	8.55	4.34	15.15	1.69	2.97	−0.005	0.01

Minerals considered were albite, actinolitic amphibole, chlorite, muscovite, biotite, dolomite, garnet, plagioclase, pyrrhotite, pyrite, anhydrite, calcite, quartz, iron carbonate, magnetite, hematite and H_2O–CO_2 fluid. Results for calculations made with an H_2S–H_2O–CO_2 fluid were compared with those for the H_2O–CO_2 fluid and found to be comparable for the situations addressed here, as very little sulphur is dissolved in solution at the conditions considered. Subsequent calculations used the H_2O–CO_2 fluid, which greatly simplifies calculations. Quartz and fluid were specified to be in excess in all calculations. Calcite, quartz, albite, pyrite, magnetite, hematite and anhydrite were assumed to be pure phases. The peristerite gap in feldspar was simulated by provision for co-existing albite and plagioclase. Activity–composition relations in the fluid were those of the van Laar asymmetric formalism described by Holland & Powell (2003). Activity–composition relations for pyrrhotite were those described in this work. Amphiboles were modelled with the ferric-bearing activity composition relations described by Diener *et al.* (2007). The enthalpy of siderite was modified slightly to enable reproduction of co-existing carbonate compositions reported by Rosenberg (1967). The carbonate models were otherwise that of White *et al.* (2003). The model for chlorite is from Holland *et al.* (1998). Otherwise, mineral activity composition models were as described by White *et al.* (2007).

Effects of pressure and temperature

The relative stabilities of carbonate-bearing mineral assemblages are sensitive to pressure, temperature and $X(CO_2)$, which makes it difficult to represent the full range of phase relations in two dimensions. Here, calculated pressure–temperature phase relations at fixed $X(CO_2)$ (Fig. 8), and *T*–$X(CO_2)$ relationships at fixed pressure (Fig. 9), are used to allow the relative effects of the different variables to be assessed.

The pressure–temperature section at a fixed $X(CO_2)$ of 0.2 (Fig. 8) is relatively simple, with few changes in topology as a function of increasing pressure until above 0.4 Gpa. It should be noted, however, that the fixed $X(CO_2)$ obscures the stabilization of carbonates relative to silicates with increasing $X(CO_2)$; this is shown in Fig. 9 and discussed below. Nevertheless, this diagram is useful because it allows changes in the silicate mineral assemblage to be assessed. The vast majority of lines have a positive dP/dT, which is typical of devolatilization reactions where entropy and volume changes are both positive. At the lowest temperatures, the stable assemblage is dolomite, iron carbonate, muscovite, pyrite, anyhydrite and albite plus quartz and fluid. The predicted presence of anhydrite is consistent with other phase equilibria studies (e.g. Evans *et al.*, 2006; Evans, 2010), but anhydrite is identified rarely in thin sections of these rocks (see Clout *et al.*, 1990 for an exception), possibly due to its poor preservation potential and/or a lack of appropriate fluid composition during metamorphism. Increasing temperature drives formation of hematite coupled with consumption of anhydrite, and then chlorite growth at temperatures that increase from around 310 °C at 0.1 GPa to 410 °C at 0.4 GPa. The anhydrite–hematite transition is trivariant and is thus, theoretically, a field in P–T space, but the width of the field is only about 0.1 °C, which is below the resolution of the figure; so, the field appears as a line.

The next reaction with increasing temperature depends on pressure, because of the differing slopes in pressure–temperature space of the low-variance fields in which sulphide–oxide and silicate–carbonate transitions take place. At the lowest pressures (< 0.12 GPa), the anhydrite–hematite transition is followed by chlorite growth, loss of iron-carbonate, calcite growth and loss of hematite coupled with growth of magnetite. Between 0.12 and 0.25 GPa, the anhydrite–hematite transition is followed by chlorite growth, as before, but loss of hematite in favour of magnetite is the next reaction, which precedes chlorite growth, loss of iron carbonate and calcite growth. Between 0.25 and 0.39 GPa, both anhydrite–hematite and hematite–magnetite transitions occur at lower temperatures than the sequence of chlorite growth, loss of iron-carbonate and calcite growth, whereas, at pressures greater than 0.39 GPa, the hematite stability field terminates and anhydrite is lost in favour of magnetite instead. This variation, not recognized previously, has the potential for use as a qualitative geobarometer.

The hematite–magnetite reaction is, like the anhydrite–hematite reaction, very narrow in P–T space. This is because the hematite–magnetite reaction is degenerate in the system NCKFMASCOSH and is effectively divariant. The narrow temperature interval over which hematite and magnetite coexist contrasts with petrological phase relations where hematite and magnetite are frequently observed in textural equilibrium (e.g. Phillips & Gibb, 1993; Evans *et al.*, 2006; Neumayr *et al.*, 2008). The most likely explanation is that fluid-rock buffering extends the stability range for the hematite plus magnetite-bearing assemblages.

Higher model temperatures drive loss of dolomite and growth of biotite. Mineral assemblages at Kalgoorlie do not contain biotite; so, the biotite-in line provides a limit on the pressures and temperatures of hydrothermal alteration, although the limits shown are sensitive to the assumed bulk-rock and fluid composition, and should be treated with caution. Other reactions that are not seen in examples from Kalgoorlie include growth of pyrrhotite at the expense of pyrite, which follows biotite-in at pressures less than 0.32 GPa and crossing of the peristerite gap, with conversion of albite to plagioclase. At pressures greater than 0.32 GPa, closure of the peristerite gap occurs at lower temperatures than the pyrite–pyrrhotite transition. The relative positions of the pyrite–pyrrhotite boundary and boundaries between the silicate mineral assemblages is pressure sensitive, and thus has the potential to be used as a geobarometer. The absence of pyrrhotite in the Golden Mile is consistent with the phase diagram; pyrrhotite-bearing greenstones, such as those at neighbouring Mount Charlotte are thought to have been formed at significantly higher temperatures than those of the Golden Mile (e.g. Bateman & Hagemann, 2004).

Amphibole is stabilized at temperatures greater than 420 °C, and the carbonate phases react out, so that the highest temperature assemblage modelled is amphibole–biotite–pyrrhotite–magnetite–quartz–plagioclase–fluid. This is equivalent to the observed pre-hydrothermal alteration assemblage if it is considered that the biotite is stabilized by the addition of hydrothermal potassium.

At the highest pressures considered (> 0.45 GPa) the amphibole- and muscovite-bearing fields converge, so that there is no longer a distinct separation between the two index minerals. The fields converge at a small divariant field with negligible width at about 480 °C and 0.45–0.5 GPa, which contains both muscovite and amphibole.

The oxide and sulphide phases observed in the Golden Mile are predicted for a rock with fixed composition in equilibrium with a H_2O–CO_2 fluid at different temperatures. However, there is little evidence for temperature gradients between the different alteration zones, or for a strong role for temperature-driven gold deposition; so, it is necessary to investigate whether variations in fluid composition can drive similar variation in the oxide/sulphide phases.

Effects of changing fluid composition

The T–$X(CO_2)$ pseudosection (Fig. 9) is more complex than the P–T pseudosection, which indicates that mineral stability is much more sensitive to temperature

and $X(CO_2)$ than to pressure. Changes to the silicate mineral assemblage at $X(CO_2)$ up to 0.5 are similar to those shown in the P–T section. At these water-rich compositions, the sequence of stable silicate minerals, with increasing temperature is muscovite–albite, muscovite–chlorite–albite, muscovite–chlorite–biotite–albite, chlorite–biotite–albite–plagioclase, chlorite–biotite–amphibole–plagioclase and biotite–amphibole–plagioclase. The main effect of increases in $X(CO_2)$ is to destabilize chlorite in favour of the ferromagnesian carbonates, dolomite and siderite, so that at $X(CO_2)$ between 0.5 and 0.7 the amphibole–chlorite–biotite field is excised, and at $X(CO_2)$ greater than 0.7 the biotite–chlorite field also disappears so that chlorite is not stable at any temperature. The majority of lines have a positive slope in T–$X(CO_2)$ space which indicates that these reactions are dominantly decarbonation reactions, although there is likely to be some degree of accompanying dehydration. A minority of lines have negative slopes, these relate to dehydration or dehydration–decarbonation phase boundaries.

The sequence of carbonate minerals with increasing $X(CO_2)$ is calcite, calcite–dolomite, dolomite and dolomite–iron carbonate. At temperatures greater than 400 °C a carbonate-free region appears at the low $X(CO_2)$ side of the figure. The changes in stability relate to transfer of iron and magnesium from chlorite to the carbonate phases with increasing $X(CO_2)$.

The sequence of oxide and sulphide phase stabilities are identical to those in the P–T section with anhydrite–pyrite, pyrite–hematite, pyrite–magnetite and pyrrhotite–magnetite stabilized with increasing temperature. The width of the fields within which the sulphide and oxide phases changes is very narrow in T–$X(CO_2)$ space, as in P–T space. However, it can be seen that buffering along the hematite–magnetite reaction in T–$X(CO_2)$ space could produce co-existing hematite and magnetite over a wider range of temperature than would be possible if $X(CO_2)$ were fixed. Indeed, buffering along the hematite–magnetite reaction is likely because this reaction is dominantly a decarbonation reaction as indicated by its positive slope. The slope of the pyrrhotite–pyrite reaction varies as a function of the mineral assemblage. This reflects the competition between silicate, carbonate and sulphide and oxide phases for the available iron, and means that an $X(CO_2)$ gradient at fixed temperature could produce the transition from pyrite to pyrrhotite and vice versa.

Mineral assemblages in iron-rich lithologies from Kalgoorlie are predicted in the fields marked in Fig. 9, and are consistent with increasing $X(CO_2)$ at constant temperature with increasing extent of alteration. M indicates potential conditions of prehydrothermal alteration, C the distal alteration, I the intermediate alteration and P the proximal alteration. However, it should be noted that changes in bulk composition driven by metasomatism are not accounted for in the figure. The assemblage in rocks from the chlorite alteration zone is predicted in a relatively narrow low-variance (trivariant) field; widespread occurrence of this mineral assemblage indicates that rock buffering of fluid composition must have operated for this assemblage to be preserved. The hematite–magnetite reaction crosses the fields of stability for the distal, intermediate and proximal assemblages; so, it is plausible that $X(CO_2)$-driven rock buffering along this reaction could have produced coexisting hematite and magnetite in equilibrium with the observed assemblages.

Temperatures are within the range proposed by White *et al.* (2003), while $X(CO_2)$ for the proximal zone, at >0.4, is higher than that obtained from fluid inclusion studies and the results of White *et al.* (2003), which are between 0.2 and 0.3. Fluid inclusion studies generally sample fluids from quartz vein material, which may not be representative of fluids that have undergone fluid–rock interaction. Additionally, White *et al.* (2003) did not include any sulphide and oxide phases in their calculations, and so lacked the temperature constraint provided by the hematite–anhydrite reaction in this study. The relatively high calculated $X(CO_2)$ values are fixed by the position of the hematite–anhydrite line. If this line occurred at lower temperatures then values more consistent with previous fluid inclusion studies would be obtained.

Ideally, it would be possible to determine the T–$X(CO_2)$ trajectory of a rock undergoing alteration from figures such as Fig. 9. This is possible for the two extreme flow regimes where fluid compositions are completely externally and internally buffered. If fluid compositions are externally buffered by infiltration of externally derived fluid then the trajectory in $X(CO_2)$ space is vertical at the value of $X(CO_2)$ of the infiltrating fluid. If $X(CO_2)$ is internally buffered, that is, it is determined by the composition of fluid released by devolatilization reactions, then the T–$X(CO_2)$ proceeds along the line of minimum fluid production, and will track through low-variance fields on a trajectory that is parallel or at a low angle to the field boundaries. Real rocks are likely to have experienced flow regimes that were not only some combination of the end-member models but also oscillated temporally between greater and lesser contributions from the two end-members in response to changes in rates of fluid production, infiltration and strain. Additionally, the $X(CO_2)$ trajectory depends on porosity, permeability and the rate of temperature increase with respect to deformation-induced fluid loss. This is because fluid composition can change significantly without much reaction if the porosity is small, so that produced fluid easily overwhelms any resident fluid and vice versa. Thus, large porosities can mimic the effects of external buffering, while smaller porosities favour internal buffering type behaviour. Given these considerations, it is impossible to unambiguously determine T–$X(CO_2)$ trajectories without specification of a number of poorly constrained parameters. Nevertheless, observed

assemblages in the Kalgoorlie rocks are broadly compatible with a flow regime in which internal buffering of fluid composition played an important role, in spite of the significant metasomatism that is observed.

Effect of variation in sulphur content

The $X(S)$–T section (Fig. 10a) was drawn to explore the sensitivity of mineral assemblages to changes in the rock bulk sulphur content. This is of interest because it allows assessment of the effects of loss of sulphur from the rock by devolatilization, or addition by sulphidation. Neither of these processes is accounted for in the T–$X(CO_2)$ section, which is drawn for a fixed bulk composition. The figure is drawn for a pressure of 0.15 GPa and an $X(CO_2)$ of 0.2. The bulk composition is identical to that used for the previous diagrams, but SO_2 is varied between 0.02 and 1 mol.%. The quantity of the O component was varied in proportion to the sulphur.

The pseudosection exhibits the same sequence of reactions as those described in previous sections; so, these are not discussed further here. The majority of the lines are flat or relatively flat, with changes of around 0–3 °C in the temperature of boundaries for sulphur contents between 0.02 and 1 mol.%. This is as expected for field boundaries associated with changes in the silicate mineral assemblage because sulphur does not participate significantly in these reactions, but slightly surprising for the pyrrhotite–pyrite boundary, as the increase in sulphur might be expected to stabilize pyrite with respect to pyrrhotite. The reaction is insufficiently low variance that the temperature of reaction is fixed by the assemblage; however, the small changes in sulphur content investigated here are insufficient to have a major effect on the temperature of the pyrite–pyrrhotite equilibrium; so, the reaction is effectively buffered. Minor sulphur-related effects are seen; the increase in sulphur mol.% increases the width of the field within which pyrrhotite and pyrite coexist, and changes in sulphur content cause minor changes in the reaction sequence. For example, at high sulphur contents, loss of iron carbonate precedes the hematite–magnetite transition with increasing temperature, whereas at low sulphur contents this sequence is reversed. Similarly, at around 430 °C, at low sulphur contents, the pyrite–pyrrhotite transition occurs within the stability field of co-existing albite and plagioclase, while at higher sulphur contents, the pyrite–pyrrhotite transition occurs in the plagioclase stability field. These changes have little effect on the overall geometry of the diagram. The insensitivity of phase boundary positions indicates that changes in observed sulphide and oxide phases are driven dominantly by temperature and fluid composition rather than by minor changes in sulphur content at the sub-weight per cent level. This is convenient because it is difficult to account for the effects of these processes on figures such as Fig. 9. This conclusion will not apply to higher degrees of sulphidation, where added sulphur combines with a significant proportion of the iron within the rock and affects the effective Mg/Mg + Fe and hence the conditions of silicate and carbonate equilibria, as discussed by Tomkins & Grundy (2009). Such rocks include the pyrite-bearing quartz veins at Kalgoorlie, where sulphur contents are up to several weight per cent. However, comprehensive examination of the metasomatism associated with such sulphidation is beyond the scope of this study.

Effect of variation in sulphur content and fluid composition

A pseudosection in $X(S)$–$X(CO_2)$ space (Fig. 10b) was drawn to enable examination of the interplay between desulphidation and sulphidation reactions, which alter the bulk sulphur in the rock, and changes in fluid $X(CO_2)$, which can be driven by devolatilization and infiltration. The SO_2 content of the rock was varied from 0.01 to 1 mol.% while the O content was varied in proportion, as above. The figure is drawn for a pressure of 0.15 GPa and a temperature of 350 °C, so as to be relevant to gold-related alteration at Kalgoorlie. The bulk composition, except for sulphur, is that shown in Table 6.

The sequence of mineral assemblages is insensitive to the sulphur content of the rock; two orders of magnitude difference in sulphur content barely affects the $X(CO_2)$ of reaction. Thus, the positions of equilibria are relatively insensitive to processes such as the loss of sulphur bearing volatiles such as H_2S, and sulphidation reactions. Preliminary investigations indicate that section geometry is more sensitive to changes in S:O ratio, and more extreme increases in sulphur content may also have additional effects, but a full discussion of this aspect of the phase relations is beyond the scope of this study.

SUMMARY

The internally consistent data set for sulphur-bearing end-members that has been derived from experimental data reproduces natural and experimental observations. Pseudosection calculations based on the new data predict the observed sequence of mineral assemblages for greenschist facies metabasalts. New constraints on the pressure dependence of the sequence of mineral reactions has the potential for use as a qualitative but retrogression-insensitive geobarometer.

The mineral assemblages observed at Kalgoorlie, Western Australia, are predicted at $X(CO_2)$ values that increase with increasing degree of hydrothermal alteration. These results are compatible with those of previous work. The sulphide and oxide minerals present depend on $X(CO_2)$. Assemblages are insensitive to the sulphur bulk content at sulphur contents between 0.01 and 1 mol.%, which means that volatilization of sulphur bearing fluids and sulphidation are unlikely to have had major effects on the stable mineral assemblage where sulphidation is not extreme. However,

higher degrees of sulphidation are likely to have a significant effect on the pressure–temperature–fluid compositions of the phase boundaries. The sequence of stable sulphide and oxide phases with increasing $X(CO_2)$ at 350 °C is pyrite–magnetite, pyrite–hematite and anhydrite–pyrite. Magnetite–pyrrhotite is predicted at temperatures greater than 410 °C. This is of particular interest because it has been proposed that such variation in sulphide and oxide phases is produced by the infiltration of multiple fluids with contrasting redox state (e.g. Neumayr *et al.*, 2008). The work presented here shows that this need not be the case.

ACKNOWLEDGEMENTS

Much of this work was funded by CSIRO Exploration and Mining during a CSIRO Postdoctoral Fellowship held by K. Evans. The work was completed under the aegis of a research and teaching fellowship at Curtin University of Technology. N. Phillips is thanked for discussion and comments. R. Frost and A. Tomkins are thanked for helpful, constructive and thought-provoking reviews. T. Wagner is thanked for comments on an earlier version of the manuscript.

REFERENCES

Adams, L.H. & Williamson, E.D., 1923. On the compressibility of minerals and rocks at high pressures. *Journal of the Franklin Institute*, **195,** 475–529.

Alcock, C.B. & Richardson, F.D., 1951. Thermodynamics of ferrous sulphide. *Nature*, **168,** 661–662.

Anderko, A., Wang, P. & Rafal, M., 2002. Electrolyte solutions: from thermodynamic and transport property models to the simulation of industrial processes. *Fluid Phase Equilibria*, **194–197,** 123–142.

Arnold, R.G., 1951. Equilibrium relations between pyrrhotite and pyrite from 325 to 743 degrees C. *Economic Geology*, **57,** 72–90.

Barin, I., 1995. *Thermochemical data of pure substances. Volume I. Ag–Kr*. VCH, New York.

Barker, W.W. & Parks, T.C., 1986. The thermodynamic properties of pyrrhotite and pyrite – a reevaluation. *Geochimica et Cosmochimica Acta*, **50,** 2185–2194.

Barton, P.B. & Toulmin, P., 1964. The electrum-tarnish method for the determination of the fugacity of sulfur in laboratory sulfide systems. *Geochemica et Cosmochimica Acta*, **28,** 619–640.

Bateman, R. & Hagemann, S., 2004. Gold mineralisation throughout about 45 Ma of Archaean orogenesis protracted: flux of gold in the Golden Mile, Yilgarn craton, Western Australia. *Mineralium Deposita*, **39,** 536–559.

Benning, L.G. & Seward, T.M., 1996. Hydrosulphide complexing of Au(I) in hydrothermal solutions from 150–400 degrees C and 500–1500 bar. *Geochimica et Cosmochimica Acta*, **60,** 1849–1871.

Birch, F., 1966. Compressibility; elastic constants. In: *Handbook of Physical Constants* (ed. Clark, S.P.), pp. 97–174. Geological Society of America Inc., New York.

Boulter, C.A., Fotios, M.G. & Phillips, G.N., 1987. The Golden Mile, Kalgoorlie – a giant gold deposit localized in ductile shear zones by structurally induced infiltration of an auriferous metamorphic fluid. *Economic Geology*, **82,** 1661–1678.

Burgmann, W.J., Urbain, G. & Frohberg, M.G., 1968. Contribution à l'étude du système fer-soufre limité au domaine du mono-sulfure de fer (pyrrhotine). *Mèmoires et Etudes Scientifiques de la Revue de Mètallurgie*, **115,** 567–578.

Cemic, L. & Kleppa, O.J., 1988. High-temperature calorimetry of sulfide systems. 3. Standard enthalpies of formation of phases in the systems Fe–Cu–S and Co–S. *Physics and Chemistry of Minerals*, **16,** 172–179.

Chase, M.W.J., 1998. *NIST–JANAF Thermochemical Tables*, 4th edn. American Chemical Society and the American Institute of Physics for the National Institute of Standards and Technology, Gaithersburg, MD.

Chase, M.W., Jr, Davies, C.A., Downey, J.R. *et al.*, 1985. JANAF thermochemical tables. *Journal of Physical and Chemical Reference Data*, **14**(Suppl. 1)**,** 1856.

Clout, J.M., Cleghorn, J.H. & Eaton, P.C., 1990. Geology of the Kalgoorlie gold field. In: *Geology of the Mineral Deposits of Australia and Papua New Guinea* (ed. Hughes, F.E.), pp. 411–431, The Australasian Institute of Mining and Metallurgy, Melbourne.

Coughlin, J.P., 1950. High-temperature heat contents of manganous sulphide, ferrous sulphide and pyrite. *American Chemical Society Journal*, **72,** 5445–5448.

Cox, J.D., Wagman, D.D. & Medvedev, V.A., 1987. *CODATA Key Values for Thermodynamics*. Hemisphere Publishing Corporation, New York.

Dickson, F.W., Shields, L.D. & Kennedy, G.C., 1962. A method for the determination of equilibrium sulfur pressures of metal sulfide reactions. *Economic Geology and the Bulletin of the Society of Economic Geologists*, **57,** 1021–1030.

Diener, J.F.A., Powell, R., White, R.W. & Holland, T.J.B., 2007. A new thermodynamic model for clino- and orthoamphiboles in the system Na_2O–CaO–FeO–MgO–Al_2O_3–SiO_2–H_2O–O. *Journal of Metamorphic Geology*, **25,** 631–656.

Etheridge, M.A., Wall, V.J. & Vernon, R.H., 1983. The role of the fluid phase during regional metamorphism and deformation. *Journal of Metamorphic Geology*, **1,** 205–226.

Evans, H.T., 1979. The thermal expansion of anhydrite to 1000 degrees C. *Physics and Chemistry of Minerals*, **4,** 77–82.

Evans, K.A., 2010. A test of the viability of fluid–wall rock interaction mechanisms for changes in opaque phase assemblage in metasedimentary rocks in the Kambalda-St. Ives goldfield, Western Australia. *Mineralium Deposita*, **45,** 207–213.

Evans, K. & Powell, R., 2006. A method for activity calculations in saline and mixed solvent solutions at elevated temperature and pressure: a framework for geological phase equilibria calculations. *Geochimica et Cosmochimica Acta*, **70,** 5488–5506.

Evans, K.A., Phillips, G.N. & Powell, R., 2006. Rock-buffering of auriferous fluids in altered rocks associated with the Golden Mile-style mineralization, Kalgoorlie gold field, Western Australia. *Economic Geology*, **101,** 805–817.

Flowers, G.C., 1979. Correction of Holloway's (1977) adaptation of the modified Redlich–Kwong equation of state for calculation of the fugacities of molecular-species in supercritical fluids of geologic interest. *Contributions to Mineralogy and Petrology*, **69,** 315–318.

Frost, B.R., 1979. Mineral equilibria involving mixed volatiles in a C–O–H fluid phase – stabilities of graphite and siderite. *American Journal of Science*, **279,** 1033–1059.

Frost, B.R., 1985. On the stability of sulfides, oxides, and native metals in serpentinite. *Journal of Petrology*, **26,** 31–63.

Grønvold, F., Stølen, S., Labban, A.K. & Westrum, E.F.J., 1991. Thermodynamics of iron sulphides. I. Heat capacity and thermodynamic properties of Fe_9S_{10} at temperatures from 5K to 740K. *The Journal of Chemical Thermodynamics*, **23,** 261–272.

Grønvold, F. & Stølen, S., 1992. Thermodynamics of iron sulphides. II. Heat capacity and thermodynamic properties of FeS and of $Fe_{0.875}S$ at temperatures from 298.15K to 1000K, of $Fe_{0.98}S$ from 298.15K to 800K and of $Fe_{0.89}S$ from 298.15K to about 650K. *The Journal of Chemical Thermodynamics*, **24,** 913–936.

Grønvold, F., Westrum, E.F.J. & Chou, C., 1959. Heat capacities and thermodynamic. Properties of the pyrrhotites FeS and $Fe_{0.877}S$ from 5 to 350K. *The Journal of Chemical Physics*, **10,** 528–531.

Ho, S.E., Groves, D.I., McNaughton, N.J. & Micucki, E.J., 1992. The source of ore fluids and solutes in Archaean lode-gold deposits of Western Australia. *Journal of Volcanology and Geothermal Research*, **50,** 173–196.

Holland, T.J.B. & Powell, R., 1990. An enlarged and updated internally consistent thermodynamic dataset with uncertainties and correlations: the system K_2O–Na_2O–CaO–MgO–MnO–FeO–Fe_2O_3–Al_2O_3–TiO_2–SiO_2–C–H_2–O_2. *Journal of Metamorphic Geology*, **8,** 89–124.

Holland, T.J.B. & Powell, R., 1991. A compensated-Redlich–Kwong (Cork) equation for volumes and fugacities. of CO_2 and H_2O in the range 1-bar to 50-Kbar and 100–1600-degrees-C. *Contributions to Mineralogy and Petrology*, **109,** 265–273.

Holland, T.J.B. & Powell, R., 1992. Plagioclase feldspars: activity-composition relations based upon Darken's quadratic formalism and Landau theory. *American Mineralogist*, **77,** 53–61.

Holland, T. & Powell, R., 1996a. Thermodynamics of order-disorder in minerals: I. Symmetric formalism applied to minerals of fixed composition. *American Mineralogist*, **81,** 1413–1424.

Holland, T. & Powell, R., 1996b. Thermodynamics of order-disorder in minerals: II. Symmetric formalism applied to solid solutions. *American Mineralogist*, **81,** 1425–1437.

Holland, T.J.B. & Powell, R., 1998. An internally consistent thermodynamic data set for phases of petrological interest. *Journal of Metamorphic Geology*, **16,** 309–343.

Holland, T. & Powell, R., 2003. Activity–composition relations for phases in petrological calculations: an asymmetric multicomponent formulation. *Contributions to Mineralogy and Petrology*, **145,** 492–501.

Holland, T., Baker, J. & Powell, R., 1998. Mixing properties and activity–composition relationships of chlorites in the system MgO–FeO–Al_2O_3–SiO_2–H_2O. *European Journal of Mineralogy*, **10,** 395–406.

Holloway, J.R., 1977. Fugacity and activity of molecular species in supercritical fluids. In: *Thermodynamics in Geology* (ed. Fraser, D.G.), pp. 161–181. D. Reidel Publishing Company, Dordrecht.

Johnson, J.W., Oelkers, E.H. & Helgeson, H.C., 1992. SUPCRT92: a software package for calculating the standard molal thermodynamic properties of minerals, gases, aqueous species and reactions from 1 to 5000 bar and 0 to 1000°C. *Computers and Geosciences*, **18,** 899–947.

King, H.E. & Prewitt, C.T., 1982. High-pressure and high-temperature polymorphism of iron sulfide (FeS). *Acta Crystallographica Section B-Structural Science*, **38,** 1877–1887.

Kishima, N., 1989. A thermodynamic study on the pyrite–pyrrhotite–magnetite–water system at 300–500-degrees-C with relevance to the fugacity concentration quotient of aqueous H_2S. *Geochimica et Cosmochimica Acta*, **53,** 2143–2155.

Kissin, S.A. & Scott, S.D., 1982. Phase-relations involving pyrrhotite below 350-degrees C. *Economic Geology*, **77,** 1739–1754.

Lin, R.Y., Ipser, H. & Chang, Y.A., 1977. Activity of sulphur in pyrrhotite at 1073K. *Metallurgical and Materials Transactions B-Process Metallurgy and Materials Processing Science*, **8B,** 345–346.

Majzlan, J., Navrotsky, A. & Neil, J.M., 2002. Energetics of anhydrite, barite, celestine, and anglesite: a high-temperature and differential scanning calorimetry study. *Geochimica et Cosmochimica Acta*, **66,** 1839–1850.

McCaig, A.M., 1988. Deep fluid circulation in fault zones. *Geology*, **16,** 867–870.

McCuaig, T.C. & Kerrich, R., 1998. *P–T–t* – deformation-fluid characteristics of lode gold deposits: evidence from alteration systematics. *Ore Geology Reviews*, **12,** 381–453.

Mills, K.C., 1974. *Thermodynamic Data for Inorganic Sulphides, Selenides and Tellurides*. Butterworths, London.

Neall, F.B. & Phillips, G.N., 1987. Fluid–wall rock interaction in an Archean hydrothermal gold deposit: a thermodynamic model for the Hunt Mine, Kambalda. Economic Geology , **82,** 1679–1694.

Neumayr, P., Walshe, J., Hagemann, S. *et al.*, 2008. Oxidized and reduced mineral assemblages in greenstone belt rocks of the St. Ives gold camp, Western Australia: vectors to high-grade ore bodies in Archaean gold deposits? *Mineralium Deposita*, **43,** 363–371.

Palin, J.M. & Xu, Y., 2000. Gilt by association? Origins of pyritic gold ores in the Victory mesothermal gold deposit, Western Australia. *Economic Geology*, **95,** 1627–1634.

Phillips, G.N., 1986. Geology and alteration in the Golden Mile, Kalgoorlie. *Economic Geology*, **81,** 779–808.

Phillips, G.N. & Brown, I.J., 1987. Host rock and fluid control on carbonate assemblages in the Golden Mile Dolerite, Kalgoorlie gold deposit, Australia. *Canadian Mineralogist*, **25,** 265–273.

Phillips, G.N. & Gibb, H.F.C., 1993. *A Century of Gold Mining at Kalgoorlie*, Key Centre in Economic Geology, Economic Geology Research Unit, Townsville, Australia.

Phillips, D.J. & Phillips, S.L., 2000. High temperature dissociation constants of HS^- and the standard thermodynamic values for S_2^-. *Journal of Chemical Engineering Data*, **45,** 981–987.

Pitzer, K.S. & Simonson, J.M., 1986. Thermodynamics of multicomponent, miscible, ionic systems – theory and equations. *Journal of Physical Chemistry*, **90,** 3005–3009.

Powell, R., 1983. Thermodynamic mixing properties of pyrrhotine, $Fe_{1-x}S$. *Mineralogical Magazine*, **47,** 437–440.

Powell, R. & Holland, T.J.B., 1985. An internally consistent dataset with uncertainties and correlations: 1. Methods and a worked example. *Journal of Metamorphic Geology*, **3,** 327–342.

Powell, R. & Holland, T., 1993. The applicability of least-squares in the extraction of thermodynamic data from experimentally bracketed mineral equilibria. *American Mineralogist*, **78,** 107–112.

Powell, R. & Holland, T.J.B., 2008. On thermobarometry. *Journal of Metamorphic Geology*, **26,** 155–179.

Powell, R., Will, T.M. & Phillips, G.N., 1991. Metamorphism in Archaean greenstone belts: calculated fluid compositions and implications for gold mineralisation. *Journal of Metamorphic Geology*, **9,** 141–150.

Powell, R., Holland, T. & Worley, B., 1998. Calculating phase diagrams involving solid solutions via non-linear equations, with examples using THERMOCALC. *Journal of Metamorphic Geology*, **16,** 577–588.

Pratt, A.R., Muir, I.J. & Nesbitt, H.W., 1994. X-ray photoelectron and auger-electron spectroscopic studies of pyrrhotite and mechanism of air oxidation. *Geochimica et Cosmochimica Acta*, **58,** 827–841.

Rau, H., 1976. Energetics of defect formation and interaction in pyrrhotite $Fe_{1-x}S$ and its homogeneity range. *Journal of Physics and Chemistry of Solids*, **37,** 425–429.

Robie, R.A., 1966. Thermodynamic properties of minerals. In: *Handbook of Physical Constants* (ed. Clark, S.P.), pp. 437–458. Geological Society of America Inc., New York.

Robie, R.A. & Hemingway, B.S., 1995. *Thermodynamic Properties of Minerals and Related Substances at 298.15 K and 1 bar (10^5* Pascals) Pressure and at Higher Temperatures. USGS, Washington, D.C.

Rosenberg, P.E., 1967. Subsolidus relations in the system $CaCO_3$–$MgCO_3$–$FeCO_3$ between 350° and 550°C. *The American Mineralogist*, **52,** 787–796.

Rosenqvist, T., 1954. A thermodynamic study of the iron, cobalt, and nickel sulphides. *Journal of the Iron and Steel Institute*, **176,** 37–57.

Schneeberg, E.P., 1973. Sulfur fugacity measurements with the electrochemical cell Ag–AgI–Ag_{2+x} + S_2. *Economic Geology*, **68,** 507–517.

Selivanov, E.N., Vershinin, A.D. & Gulyaeva, R.I., 2003. Thermal expansion of troilite and pyrrhotine in helium and air. *Inorganic Materials*, **39,** 1097–1102.

Shock, E.L. & Helgeson, H.C., 1988. Calculation of the thermodynamic and transport-properties of aqueous species at high-pressures and temperatures – correlation algorithms for ionic species and equation of state predictions to 5-kB and 1000-degrees-C. *Geochimica Et Cosmochimica Acta*, **52,** 2009–2036.

Shvarov, Y. & Bastrakov, E., 1999. HCH: A Software Package for Geochemical Equilibrium Modelling. User's Guide. Australian Geological Survey Organisation, Canberra.

Skinner, B.J., 1966. Thermal expansion. In: *Handbook of Physical Constants* (ed. Clark, S.P.), pp. 75–96. Geological Society of America Inc., New York.

Skinner, W.M., Nesbitt, H.W. & Pratt, A.R., 2004. XPS identification of bulk hole defects and itinerant Fe 3d electrons in natural troilite (FeS). *Geochimica et Cosmochimica Acta*, **68,** 2259–2263.

Suleimenov, O.M. & Seward, T.M., 1997. A spectrophotometric study of hydrogen sulphide ionisation in aqueous solutions to 350 degrees C. *Geochimica et Cosmochimica Acta*, **61,** 5187–5198.

Taylor, L.A., 1970. Low temperature phase relations in the Fe–S system. *Carnegie Institute Washington Yearbook*, **69,** 259–270.

Tenailleau, C., Etschmann, B., Wang, H., Pring, A., Grguric, B.A. & Studer, A., 2005. Thermal expansion of troilite and pyrrhotite determined by *in situ* cooling (873 to 373 K) neutron powder diffraction measurements. *Mineralogical Magazine*, **69,** 205–216.

Tomkins, A.G. & Grundy, C., 2009. Upper temperature limits of orogenic gold deposit formation: constraints from the granulite-hosted Griffin's Find deposit, Yilgarn Craton. *Economic Geology*, **104,** 669–685.

Tomkins, A., Pattison, D.R.M. & Frost, B.R., 2007. On the initiation of metamorphic sulfide anatexis. *Journal of Petrology*, **48,** 511–535.

Toulmin, P. & Barton, P.B., 1964. Thermodynamic study of pyrite and pyrrhotite. *Geochimica et Cosmochimica Acta*, **28,** 641–671.

Urakawa, S., Someya, K., Terasaki, H. *et al*., 2004. Phase relationships and equations of state for FeS at high pressures and temperatures and implications for the internal structure of Mars. *Physics of the Earth and Planetary Interiors*, **143/144,** 469–479.

Waldner, P. & Pelton, A.D., 2005. Thermodynamic modeling of the Fe–S system. *Journal of Phase Equilibria and Diffusion*, **26,** 23–38.

Wang, H.P. & Salveson, I., 2005. A review on the mineral chemistry of the non-stoichiometric iron sulphide, $Fe_{1-x}S$ ($0 < x < 0.125$): polymorphs, phase relations and transitions, electronic and magnetic structures. *Phase Transitions*, **78,** 547–567.

Wang, P., Anderko, A. & Young, E.D., 2002. A speciation-based model for mixed-solvent electrolyte systems. *Fluid Phase Equilibria*, **203,** 141–176.

White, R.W., Powell, R. & Phillips, G.N., 2003. A mineral equilibria study of the hydrothermal alteration in mafic greenschist facies rocks at Kalgoorlie, Western Australia. *Journal of Metamorphic Geology*, **21,** 455–468.

White, R.W., Powell, R. & Holland, T.J.B., 2007. Progress relating to calculation of partial melting equilibria for metapelites. *Journal of Metamorphic Geology*, **25,** 511–527.

Yund, R.A. & Hall, H.T., 1970. Kinetics and mechanism of pyrite exsolution from pyrrhotite. *Journal of Petrology*, **11,** 381–404.

Received 18 September 2009; revision accepted 5 May 2010.